

Metal-poor Stars Observed with the Automated Planet Finder Telescope. II. Chemodynamical Analysis of Six Low-Metallicity Stars in the Halo System of the Milky Way

MOHAMMAD K. MARDINI,^{1,2} VINICIUS M. PLACCO,^{3,4} ALI TAANI,⁵ HAINING LI,¹ AND GANG ZHAO^{1,2}

¹*Key Lab of Optical Astronomy, National Astronomical Observatories, Chinese Academy of Sciences, Beijing, China*

²*School of Astronomy and Space Science, University of Chinese Academy of Sciences, Beijing, China*

³*Department of Physics, University of Notre Dame, Notre Dame, IN 46556, USA*

⁴*JINA Center for the Evolution of the Elements, USA*

⁵*Physics Department, Faculty of Science, Al-Balqa Applied University, Al-Salt, Jordan*

ABSTRACT

In this work, we study the chemical compositions and kinematic properties of six metal-poor stars with $[\text{Fe}/\text{H}] < -2.5$ in the Galactic halo. From high-resolution ($R \sim 110,000$) spectroscopic observations obtained with the Lick/APF, we determined individual abundances for up to 23 elements, to quantitatively evaluate our sample. We identify two carbon-enhanced metal-poor stars (J1630+0953 and J2216+0246) without enhancement in neutron-capture elements (CEMP-no stars), while the rest of our sample stars are carbon-intermediate. By comparing the light-element abundances of the CEMP stars with predicted yields from non-rotating zero-metallicity massive-star models, we find that possible the progenitors of J1630+0953 and J2216+0246 could be in the 13-25 M_{\odot} mass range, with explosion energies $0.3\text{--}1.8 \times 10^{51}$ erg. In addition, the detectable abundance ratios of light and heavy elements suggest that our sample stars are likely formed from a well-mixed gas cloud, which is consistent with previous studies. We also present a kinematic analysis, which suggests that most of our program stars likely **belong to** the inner-halo population, with orbits passing as close as ~ 2.9 kpc from the Galactic center. We discuss the implications of these results on the critical constraints on the origin and evolution of CEMP stars, as well as the nature of the Population III progenitors of the lowest metallicity stars in our Galaxy.

Keywords: Galaxy: halo—techniques: spectroscopy—stars:fundamental parameters—stars: abundances—stars: atmospheres—stars: kinematics and dynamics — stars: Population II— stars: chemically peculiar

1. INTRODUCTION

The detailed study of the chemical composition of metal-poor stars in the Milky Way greatly contributes to our understanding of Galactic chemical evolution (GCE). The best candidates for such studies are the very metal-poor ($[\text{Fe}/\text{H}] < -2.0$, hereafter VMP), extremely metal-poor ($[\text{Fe}/\text{H}] < -3.0$, hereafter EMP), and ultra metal-poor ($[\text{Fe}/\text{H}] < -4.0$, hereafter UMP) stars. These second-generation objects (Pop II) have formed from low-metallicity gas clouds at redshift $\gtrsim 6$ (see Frebel 2018, and references therein). Each element

in their atmosphere can potentially help us understand the underlying physical processes by which our Galaxy evolved chemically, considering that each element might follow different nucleosynthesis pathway(s).

A number of previous observational studies have indicated that carbon is omnipresent in the early universe (Beers & Christlieb 2005; Aoki et al. 2007; Hansen et al. 2016a; Placco et al. 2016; Cruz et al. 2018; Caffau et al. 2018). Hence, the discovery and analysis of carbon-enhanced metal-poor stars ($[\text{C}/\text{Fe}] \geq 0.7$ ¹ hereafter CEMP), suggest that this substantial enhancement could be closely linked to their formation. In addition

Corresponding author:
Haining Li [lhn@nao.cas.cn]
Gang Zhao [gzhao@nao.cas.cn]

¹ Using Aoki et al. (2007), as the criterion for carbon enhancement.

to carbon enhancement, different abundance ratios of neutron-capture elements are often used to distinguish the unique nature of CEMP stars: CEMP-s ($[\text{C}/\text{Fe}] \geq +0.7$, $[\text{Ba}/\text{Fe}] > +1.0$, and $[\text{Ba}/\text{Eu}] > +0.5$), CEMP-r/s ($[\text{C}/\text{Fe}] \geq +0.7$ and $0.0 < [\text{Ba}/\text{Eu}] < +0.5$), CEMP-r ($[\text{C}/\text{Fe}] \geq +0.7$ and $[\text{Eu}/\text{Fe}] > +1.0$), and CEMP-no ($[\text{C}/\text{Fe}] \geq +0.7$ and $[\text{Ba}/\text{Fe}] < 0.0$).

The CEMP-s and CEMP-no subclasses represent the predominant populations of the CEMP stars (Beers & Christlieb 2005; Aoki et al. 2007; Hansen et al. 2016a; Yoon et al. 2016). The chemical patterns associated with CEMP-s stars (high enhancement in carbon and s-process elements) can arise from an intrinsic (self-enrichment) or an extrinsic (mass transfer from now white dwarf companion) process. Nevertheless, the overabundance of s-process elements (e.g., $[\text{Ba}/\text{Fe}] > +1.0$) support the matter accretion from an asymptotic giant branch (AGB) companion. These s-process elements (e.g., Sr, Ba, and Ce) are believed to be synthesized in low- to intermediate-mass stars (1 to 3 M_{\odot}), with low neutron densities ($n_n \approx 10^6 \text{ cm}^{-3} - 10^{10} \text{ cm}^{-3}$) and $^{13}\text{C}(\alpha, n)^{16}\text{O}$ as the main source of neutrons, which are eventually transferred and mixed into the atmosphere of the long-lived companion (observed as a CEMP-s star, Lucatello et al. 2005; Starkenburg et al. 2014).

CEMP-r/s and CEMP-r are much less frequent when compared with other subclasses. The origin of their enhancement (in r-process elements) is still widely debated. In contrast to the s-process elements, a high neutron density ($n_n > 10^{22} \text{ cm}^{-3}$) is the key to synthesize these unstable neutron-rich isotopes (e.g., Eu, Os, and Ir). In the past, there have been many astrophysical sites proposed for r-process production. Still a few can provide such high neutron density environment (see Thielemann et al. 2017, and references therein). Presently, the possible sites are confined to magnetorotationally jet-driven supernovae (SN), core-collapse SN, neutron stars mergers, and neutron star-black hole mergers (e.g., Frebel 2018).

The CEMP-no stars, which are believed to be the direct descendants of objects formed shortly after the big bang (Pop III), (Ito et al. 2013; Placco et al. 2014b; Hansen et al. 2016b), dominate the lowest-metallicity regime (e.g., Christlieb et al. 2002; Frebel et al. 2005; Caffau et al. 2011; Keller et al. 2014; Starkenburg et al. 2018) and reside in the main-sequence, subgiants, or red giant phase. Their evolutionary stages and chemical patterns (excess in carbon with low abundances or absence of neutron-capture elements) suggest that a binary companion or self-enrichment are unlikely the sources of their chemical patterns. Therefore, a distinct enrichment channel may have taken place (e.g., Starken-

burg et al. 2014; Hansen et al. 2016c). A spinstar is one possible candidate; these rapidly rotating massive ultra metal-poor ($[\text{Fe}/\text{H}] < -6.0$) stars can produce large amounts of carbon (Meynet et al. 2006; Hirschi 2007; Frischknecht et al. 2012; Maeder et al. 2015). Another proposed scenario for the carbon enhancement is pollution from faint supernovae associated with Pop III stars, with mixing-and-fallback (Umeda & Nomoto 2003; Tominaga et al. 2007; Heger & Woosley 2010; Nomoto et al. 2013; Tominaga et al. 2014; Ezzeddine et al. 2019). This faint SN ejects less iron and thus increases the $[\text{C}/\text{Fe}]$ ratio, as they do not have enough energy to eject all its material into its surroundings. Therefore, only the outer layers with the lightest elements are ejected while the inner part falls back onto the neutron star or black hole. At present, none of the above scenarios can explain the full chemical patterns that have been observed in CEMP-no stars. In general, the unique chemical patterns observed in the sub-classes of CEMP stars result from the differences in the astrophysical sites responsible for the nucleosynthesis products they now mixed in their atmospheres.

The Milky Way galaxy has three main components (with respect to its visible matter): the bulge (a very luminous and dense structure, hosting ongoing star formation and the Galactic supermassive black hole), the disk (a flattened region surrounding the bulge, hosting young stars), and the halo (an extend structure, primarily containing old field stars). **Metal-poor stars reside primarily in the Galactic halo system, which is believed to have at least two extended regions (the inner-halo and the outer-halo), with different metallicity distributions, kinematics, and spatial density profiles (e.g., Beers et al. 2012).** The halo system also hosts several stellar streams, overdensities (Grillmair 2009), and a recently discovered large structure in the inner region, product of a past merger event (Helmi et al. 2018). **The outer halo exhibits a fraction of CEMP stars twice as large as the inner halo in the metallicity interval $-2.5 < [\text{Fe}/\text{H}] < -2.0$.** Such an increase in frequency of CEMP stars can be explained as a population-driven effect, due to the fact that the outer halo is the dominant component at large distances from the galactic plane and at metallicities $[\text{Fe}/\text{H}] < -2.0$. More recently, many studies have suggested that the relative numbers of CEMP-no stars compared to CEMP-s stars are found to vary between the inner- and outer-halo (Carollo et al. 2014; Beers et al. 2017; Yoon et al.

2018; Mardini et al. 2019). Based on the stellar distances, those authors and many others suggested that the frequency of the CEMP-no stars is higher in the outer halo, while the frequency of the CEMP-s stars is higher in the inner halo.

In this paper, we report on the discovery of six stars with $[\text{Fe}/\text{H}] < -2.5$ selected from the LAMOST database, including two CEMP stars. This is a continuation of the work presented in Mardini et al. (2019, hereafter Paper I). By analyzing the chemical abundances and kinematics of the sample stars, we are able to establish their inner/outer halo membership and provide hints on their origin. In addition, we can constrain the nature of the Pop III progenitors of the lowest metallicity stars in our sample. This paper is outlined as follows: the target selection and observations are described in Section 2. Section 3 discusses the determination of stellar parameters. Our abundance analysis is presented in Section 4. We discuss our results, chemical peculiarities, possible progenitors, and kinematics in Section 5. Our conclusions are given in Section 6.

2. TARGET SELECTION AND OBSERVATIONS.

Our target stars were selected according to their corresponding Lick indices. We used medium-resolution ($R \sim 2,000$) spectra from the third data release (DR3²) of the Large Sky Area Multi-Object Fiber Spectroscopic Telescope (LAMOST) survey (Zhao et al. 2006, 2012; Cui et al. 2012) to estimate their metallicities. High-resolution ($R \sim 110,000$) spectroscopic follow-up was carried out, in order to confirm their low-metallicity nature and to explore their elemental abundances in detail.

2.1. High-resolution Observations

High-resolution spectroscopic observations for 12 stars were carried out using the Levy Spectrometer (optical echelle spectrometer Vogt et al. 2014) on the Automated Planet Finder (APF) Telescope at Lick Observatory. The observing setup included a 0.5" slit, yielding a resolving power of $R \sim 110,000$ across wavelength range of 3730-9989 Å, with an average S/N \sim 35 per pixel at 4500 Å (using 4 \times 30 minutes exposure times). For more information about the target selection and observations we refer the reader to Paper I. These high-resolution spectroscopic data were reduced through standard echelle data reduction procedures (e.g., bias subtraction, flat-fielding), using the Image Reduction and Analysis Facility (IRAF; Tody 1986, 1993). Six stars have been studied and reported in Paper I. In this paper, we present the remaining stars. Table 1 lists the observational de-

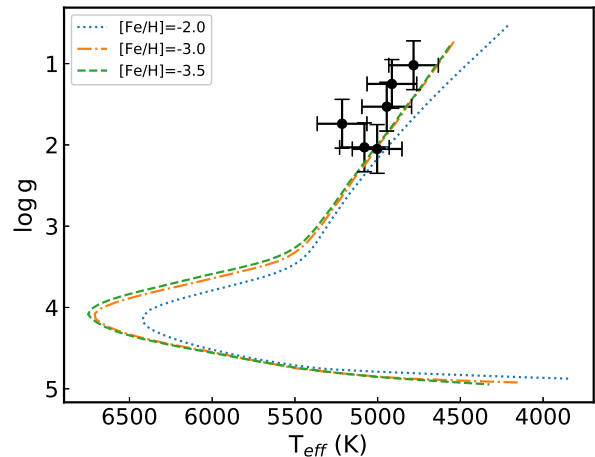


Figure 1. The adopted T_{eff} and $\log g$ of our sample stars displayed with a 12 Gyr, $[\alpha/\text{Fe}] = +0.4$, and $[\text{Fe}/\text{H}] = -2.5$, -3.0 , and -3.5 Yale-Yonsei isochrones taken from Demarque et al. (2004).

tails of these stars. Our observed radial velocities (RV) were measured by cross-correlating the high-resolution reduced spectra against synthesized templates of the same spectral type, making use of the Mg I triplet at 5160-5190 Å. These values are also listed in Table 1.

2.2. Equivalent Widths

We adopted a combined line list from Aoki et al. (2013b) and Frebel et al. (2013), for elements with $Z \leq 30$ (with the exception of carbon and nitrogen, $Z = 6$ and 7, respectively). We rejected all Fe I lines with excitation potential lower than 1.2 eV, since these lines may suffer from non-local thermodynamic equilibrium (NLTE) effects and yield abundances that are not in agreement with the ones calculated from higher excitation Fe I lines (e.g., Magain & Zhao 1996; Cohen et al. 2008). For the remaining elements considered in this study (e.g., Sr II), we adopted atomic data from the linemake code³.

The equivalent widths for the high-resolution spectra were measured using an automatic IDL routine (Kang & Lee 2015) that fits Gaussian/Voigt profiles to the selected lines, with expected errors of $\sim 1\text{mÅ}$. We visually examine each line and rejected blended lines or those with or uncertain continuum placement. The equivalent widths values are listed in Table 2.

3. STELLAR PARAMETERS

² <http://dr3.lamost.org>

³ <https://github.com/vmplacco/linemake>

The determination of atmospheric parameters, using photometric or spectroscopic data, is essential to perform a detailed chemical abundances analysis (Alonso et al. 1999; Ramírez & Meléndez 2005; Casagrande et al. 2010; Frebel et al. 2013; Mashonkina et al. 2017). However, it is well known that the ionization equilibrium of Fe I absorption features (spectroscopic method), leads to underestimated $\log g$ and T_{eff} (e.g., see Frebel et al. 2013; Mashonkina et al. 2017, and references therein).

We determined the atmospheric parameters for our target stars using a number of available methods. We adopt the atmospheric parameters (corrected values), derived based on the explicit method presented by Frebel et al. (2013). This method corrects the usually expected systematic offsets between the spectroscopic and photometric effective temperatures. This exercise increases the determined spectroscopic T_{eff} (initial values) up to several hundred degrees, and thus achieve better agreement with values determined by other methods. These stellar atmospheric parameters are listed in Table 3.

3.1. Effective Temperature

We determined the effective temperature for our sample stars by minimizing the trend between the derived abundance and excitation potentials of Fe I lines. Moreover, we make use of the available colors (UCAC4, Zacharias et al. 2013 and 2MASS, Skrutskie et al. 2006) along with the empirical calibrations of Casagrande et al. (2010) to estimate photometric T_{eff} . These T_{eff} values (photometric and spectroscopic) agree within typical uncertainties (± 150 K). In addition, we cross-matched our sample stars with Gaia DR2 (Gaia Collaboration et al. 2018) and find that Gaia DR2 values agree well with our derived values. These derived values together with T_{eff} taken from Gaia DR2 are listed in Table 3.

3.2. Surface Gravity and Microturbulence

We determined the surface gravities by minimizing the offset between the derived abundances of Fe I and Fe II lines. Moreover, we cross-matched our sample stars against the distances catalogue of Bailer-Jones et al. (2018), to estimate $\log g$ from the distance modulus.

$$\log \frac{g}{g_{\odot}} = \log \frac{M}{M_{\odot}} + 4 \log \frac{T_{\text{eff}}}{T_{\text{eff}\odot}} + 0.4(M_{\text{bol}} - M_{\text{bol}\odot})$$

$$M_{\text{bol}} = V + BC_V + 5 \log \varpi + 5$$

where M is the stellar mass, assumed to be $M/M_{\odot} = 0.8$, BC_V is the bolometric correction (determined based on Casagrande & Vandenberg (2014, 2018a,b)), V is the visual magnitude, ϖ is the parallax, $E(B-V)$ is the Color excess (adopted from Schlegel et al. (1998)⁴), and M_{bol} is the absolute bolometric magnitude. The different $\log g$ values (distance modulus and spectroscopic) agree within the typical uncertainty (± 0.3 dex).

Finally, we determined the microturbulence velocities (ξ) by removing any trend between the calculated abundances of Fe I lines and the associated EWs. Figure 1 shows the determined $\log g$ as a function of T_{eff} , for our sample stars, overlaid with 12 Gyr Yale-Yonsei isochrones (Demarque et al. 2004), as a reference. The error bars denote ± 150 K and ± 0.3 cgs (1σ errors of T_{eff} and $\log g$, respectively).

4. ABUNDANCE ANALYSIS

We employed 1D stellar atmosphere models from Castelli & Kurucz (2003) and an updated version of the stellar code MOOG (Snedden 1973; Sobeck et al. 2011; Adamow 2017) to determine our LTE chemical abundances. We used the measured EWs of the non-blended lines, with reliable continuum normalization, to perform a standard LTE abundance analysis. At the same time, we use spectral synthesis to determine abundances for blended lines, molecular bands, and neutron-capture elements. Table 4 presents the derived LTE abundances. We adopted the solar abundances from Asplund et al. (2009) to calculate the final elemental abundances and $[X/\text{Fe}]$ ratios.

4.1. Carbon and Nitrogen

We determined the carbon abundances in our sample stars from the molecular CH G band around 4247 Å. Figure 2 shows the spectral synthesis of the carbon abundance determination for J1630+0953 (upper left panel). The black filled circles represent the observed data, the solid blue line shows the best abundance fit, and the orange dashed and green dotted lines show the upper and lower abundances fits, respectively. We use these lines to estimate the uncertainty of the carbon abundance determination. The lower panel of Figure 2 shows residuals of $< 2\%$ between J1630+0953 data and our best fit for the CH G region.

The surface chemical abundances of low mass stars ($\sim 1 M_{\odot}$) are subject to change by the first dredge-up at the beginning of the red giant branch (RGB). The effects of this stellar evolution phase can be noticed (spectroscopically) by a lower observed ratio of $^{12}\text{C}/^{13}\text{C}$

⁴ <https://irsa.ipac.caltech.edu/applications/DUST>

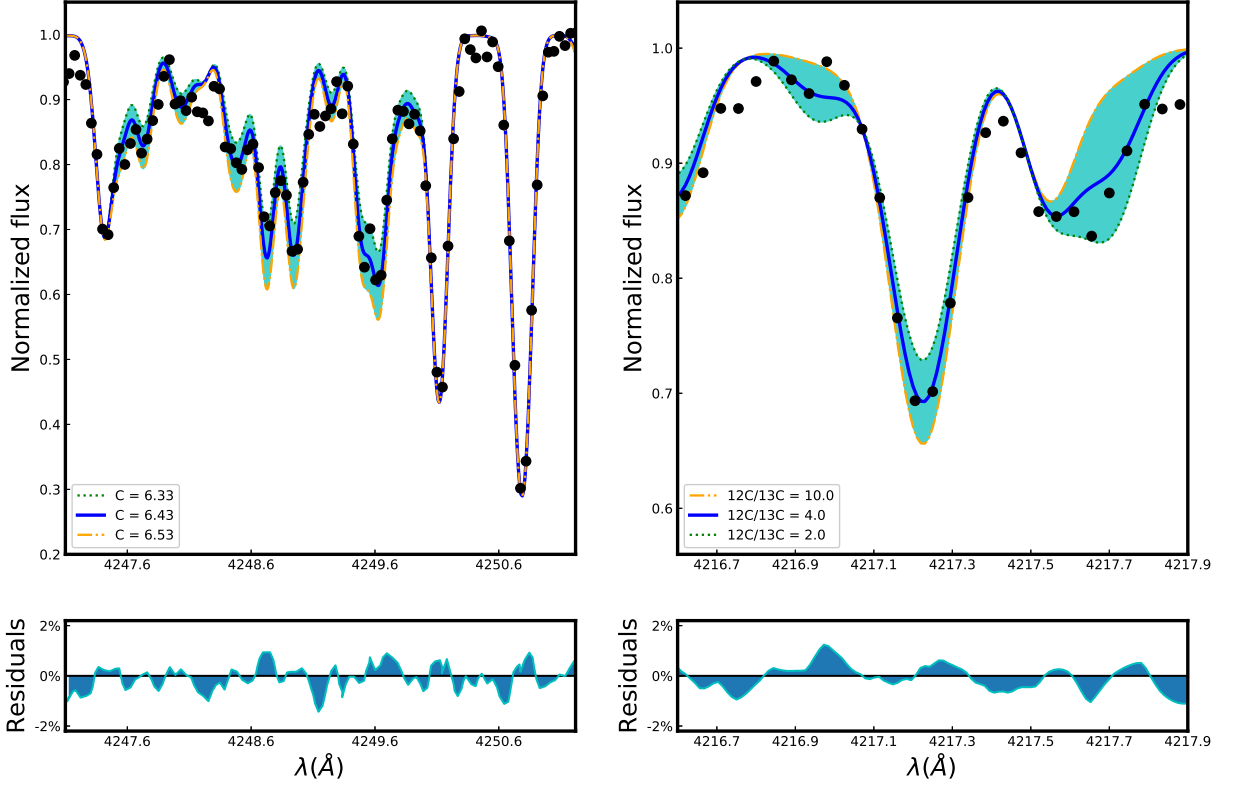


Figure 2. Left panel: Section of the spectrum for J1630+0953 near the CH G band. The filled black circles show the observed data, the solid blue line is the best abundance fit, the green dotted line represents the upper abundance, and the orange dot-dashed line represents the lower abundance. The cyan shaded area encloses a 0.2 dex difference in $\log(C)$. The right panel shows the determination of the carbon isotopic fractions ($^{12}\text{C}/^{13}\text{C}$). The filled black circles show the observed data, the solid blue line is the best fractional fit. The lower panels represent the residuals between the best fit and observed data.

and C/N (Iben 1965). The solar carbon isotopic ratio ($^{12}\text{C}/^{13}\text{C}$ ratio = 89, Asplund et al. 2009) is expected to decrease into values between 18 and 26 (e.g., Charbonnel 1994), and such enhancement in ^{13}C can be used as an indicator of the degree of the mixing processes in the outer layers of RGB stars.

To determine the carbon isotopic ($^{12}\text{C}/^{13}\text{C}$) ratios in our sample stars, we fixed the carbon abundance (e.g., $\log \epsilon(C) = 6.13$, for J1630+0953) for the CH features around 4217 Å, and then alter the isotopic ratio to achieve a best fit ($^{12}\text{C}/^{13}\text{C} = 4$, for J1630+0953). Low $^{12}\text{C}/^{13}\text{C}$ ratios suggest that a significant amount of ^{12}C has been converted into ^{13}C . In addition, a considerable amount of carbon has been converted into nitrogen. The upper right panel of Figure 2 shows the determination of the carbon isotopic ratio. The black filled circles represent the observed data, the solid blue line shows the best carbon isotopic ratio fit, with lower (green dotted) and

upper (orange dashed) limits. The lower panel shows residuals of $< 2\%$ between the observed data and the best fit ratio ($^{12}\text{C}/^{13}\text{C} = 4$) at wavelength ~ 4217 Å.

We investigate the nitrogen bands (CN) at 4215 Å and 6971 Å to determine nitrogen abundances for our sample stars. Only the J1630+0953 spectrum shows reliable features and consistent abundances.

4.2. Light Elements: from Na to Zn

We used two lines (Na I at 5889 and 5895 Å) to determine Na abundances, five lines (4703, 5172, 5183, 5528, and 5711 Å) to derive Mg abundances, and one reliable line at 4379.23 Å to derive V abundances. Moreover, we used 18 Ca I lines, 26 Ti lines (Ti I and Ti II), six Sc II lines, five Cr I lines, six Sc II lines, three Co II lines, five Ni I lines, and one Zn II line to determine the abundances for those species.

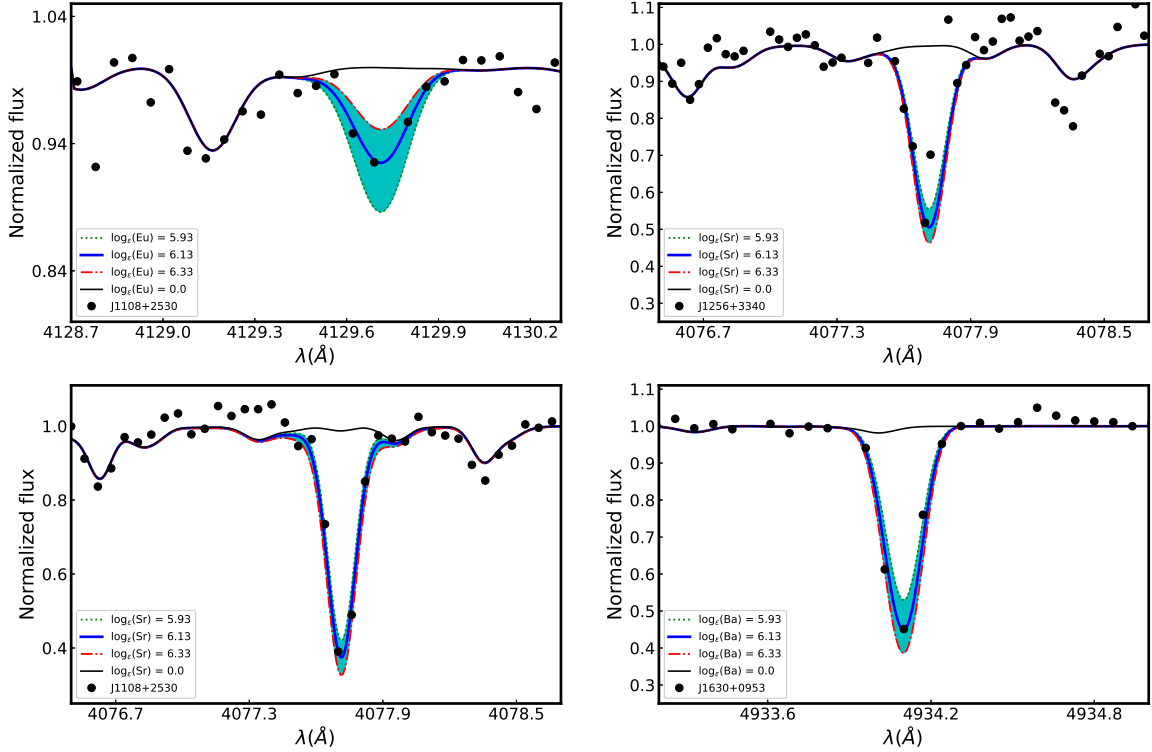


Figure 3. Demonstration examples of our spectrum synthesis analysis. Black filled circles denote portions of J1108+2530, J1256+3340, and J1630+0953 spectra. Blue solid lines denote the best-fit, while the dotted and dash-dotted lines denote the abundance variations used to estimate uncertainties.

4.3. Neutron-capture Elements

We used spectral synthesis to derive abundances for the neutron-capture elements in our sample stars: one Sr II line at 4077 Å, three Y II lines, four Ba II lines, one Zr II line, three La II lines, four Ce II lines, two Pr II lines, eight Nd II lines, two Sm II lines, and one Eu II line. Figure 3 demonstrates our spectral-synthesis fittings. The uncertainties are estimated by using same method described for carbon.

4.4. Uncertainties of Stellar Parameters and Abundances

We tested the robustness of the determined elemental abundances by altering one atmospheric parameter (T_{eff} , $\log g$, and ξ) at a time within their associated uncertainty (100 K, 0.3 dex, and 0.3 km s⁻¹, respectively). Table 5 shows the effect of this procedure on the abundances of J1630+0953, as an illustrative example. The derived chemical abundances of J1630+0953 have an overall average uncertainty of 0.2 dex. Nonetheless, we neglect the uncertainties arising from the choice of

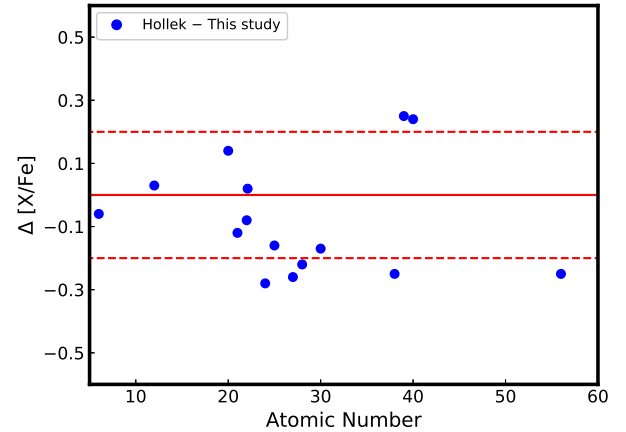


Figure 4. Elemental abundance differences of J0326+0202, as a function of the atomic number. The solid line refers to zero elemental abundance difference and the dashed lines refer to ± 0.2 dex deviations.

the atmospheric model (see Castelli & Kurucz 2003) and

the EWs measurements, because they result in negligible systematic errors, compared with the errors on the atmospheric parameters. (e.g., [Frebel et al. 2005](#); [Aoki et al. 2006](#)).

The elemental abundances of J0326+0202 have been discussed by [Hollek et al. \(2011\)](#), who analyzed a high-resolution spectrum ($R \sim 35,000$) obtained using the Magellan/MIKE. Figure 4 shows the differences between the abundances in common derived in this work and [Hollek et al. \(2011\)](#). We attribute the differences to the use of different stellar parameters ([Hollek et al. 2011](#), used $T_{\text{eff}}=4775$ K, $\log g=1.20$ dex, $[\text{Fe}/\text{H}]=-3.32$ dex, and $\xi=1.80$ kms^{-1}), different atomic data, and different techniques (equivalent width vs. spectrum synthesis).

5. RESULTS AND DISCUSSION

5.1. Chemical Abundance Comparison with Literature Data

To identify any possible chemical peculiarities in our sample, we compared our determinations with data from the literature. Figure 5 shows some of the light-element abundances, compared to C-normal stars taken from [Yong et al. \(2013\)](#). The detectable light-elements have similar abundance ratios to those reported in literature halo stars, suggesting that our sample stars have been likely formed from a well-mixed gas cloud.

All our sample stars have been evolved into the red giant branch (see Figure 1), suggesting that some internal mixing occurred and thus the atmospheric carbon abundances have been altered. [Placco et al. \(2014a\)](#) studied a sample of 505 metal-poor stars and developed a correction procedure that recovers the initial atmospheric carbon abundance. These corrections are listed in Table 4. We obtained high $[\text{C}/\text{Fe}]_{\text{corr}}$ values for J1630+0953 and J2216+0246 ($[\text{C}/\text{Fe}]_{\text{corr}} = +0.62$ and 0.42 dex, respectively), which brings the final abundances to $[\text{C}/\text{Fe}]=1.26$ and 0.70 . From these final values and the definition of the CEMP stars adopted from [Aoki et al. \(2007, CEMP, \$\[\text{C}/\text{Fe}\] \geq 0.7\$ \)](#), we classify J1630+0953 and J2216+0246 as carbon-enhanced metal-poor stars, while the rest of our program stars are carbon-intermediate.

The substantial depletion of carbon in J1630+0953 and J2216+0246 suggests that the chemical patterns observed in these two stars should be accompanied with nitrogen enhancement. However, we were only able to detect nitrogen in the spectrum of J1630+0953 ($[\text{N}/\text{Fe}]=0.88$), which is in line with its evolutionary status, while J2216+0246 spectrum show no reliable CN features.

We have determined chemical abundances for up to nine neutron-capture elements in our sample stars. Of particular interest, the observed Sr and Ba abundances could help us better understand their nucleosynthesis pathway(s), considering that Sr (first s-process peak) may be synthesized by the main or weak s-process, while Ba (second s-process peak) primarily synthesized by the main s-process ([Qian & Wasserburg 2003, 2008](#); [Andrievsky et al. 2011](#); [Hansen et al. 2014](#)). Furthermore, [Cristallo et al. \(2009, 2011\)](#) and [Lugaro et al. \(2012\)](#) predicted that low and high $[\text{Sr}/\text{Ba}]$ ratios could help discriminate between low-mass and massive metal-poor AGB stars, respectively. This further suggests that the production of Sr and Ba are linked to various astrophysical sites. On the other hand, [Aoki et al. \(2013a\)](#) suggested that these elements could be synthesized in the same event, and the observed $[\text{Sr}/\text{Ba}]$ ratios can be explained by the stars collapse time into a black-hole.

Figure 6 shows the $[\text{Sr}/\text{Ba}]$ abundance ratios of our program stars (filled red stars) and carbon-normal stars from [François et al. \(2007\)](#) (green open circles) [Yong et al. \(2013\)](#) (blue open circles), as a function of $[\text{Ba}/\text{Fe}]$. All of the sample stars show no significant differences from the trends presented by [François et al. \(2007\)](#) and [Yong et al. \(2013\)](#). However, abundances from elements in the first s-process peak in J0326+0202 ($[\text{Sr}/\text{Ba}] = 0.14$) and J1413+1727 ($[\text{Sr}/\text{Ba}] = 0.20$) appear to be enriched more than the second peak, thus an additional process is required to explain these high $[\text{Sr}/\text{Ba}]$ ratios. J1630+0953 and J2216+0246 satisfied the CEMP definition ($[\text{C}/\text{Fe}] \geq 0.7$; [Aoki et al. 2007](#)). In addition, we determined low Ba abundances ($[\text{Ba}/\text{Fe}] < 0.0$) for these stars (see Table 4). Therefore, J1630+0953 and J2216+0246 can be classified as CEMP-no stars (see [Beers & Christlieb 2005](#); [Aoki et al. 2007](#); [Placco et al. 2014a](#), Section 1, and Figure 6).

By comparing the observed neutron-capture abundance patterns in our sample stars with the solar system (SS) r- and s-fractions, we can gain insights into the nature of their heavy element enrichment. Figure 7 shows the heavy element abundance patterns of our sample stars compared with the SS r- and s-fractions, adopted from [Burris et al. \(2000\)](#). The SS s-process components are normalized to match the observed Ba (solid line), and the SS r-process patterns are normalized to match the observed Eu (dotted line). The derived abundances for Sr, Y, and Zr (within observational errors) in J0326+0202 seem to be inconsistent with the SS distributions. These discrepancies require an additional process(es) to interpret the overall neutron-capture abundance pattern observed in this star. However, these elements seem to be consistent with the SS

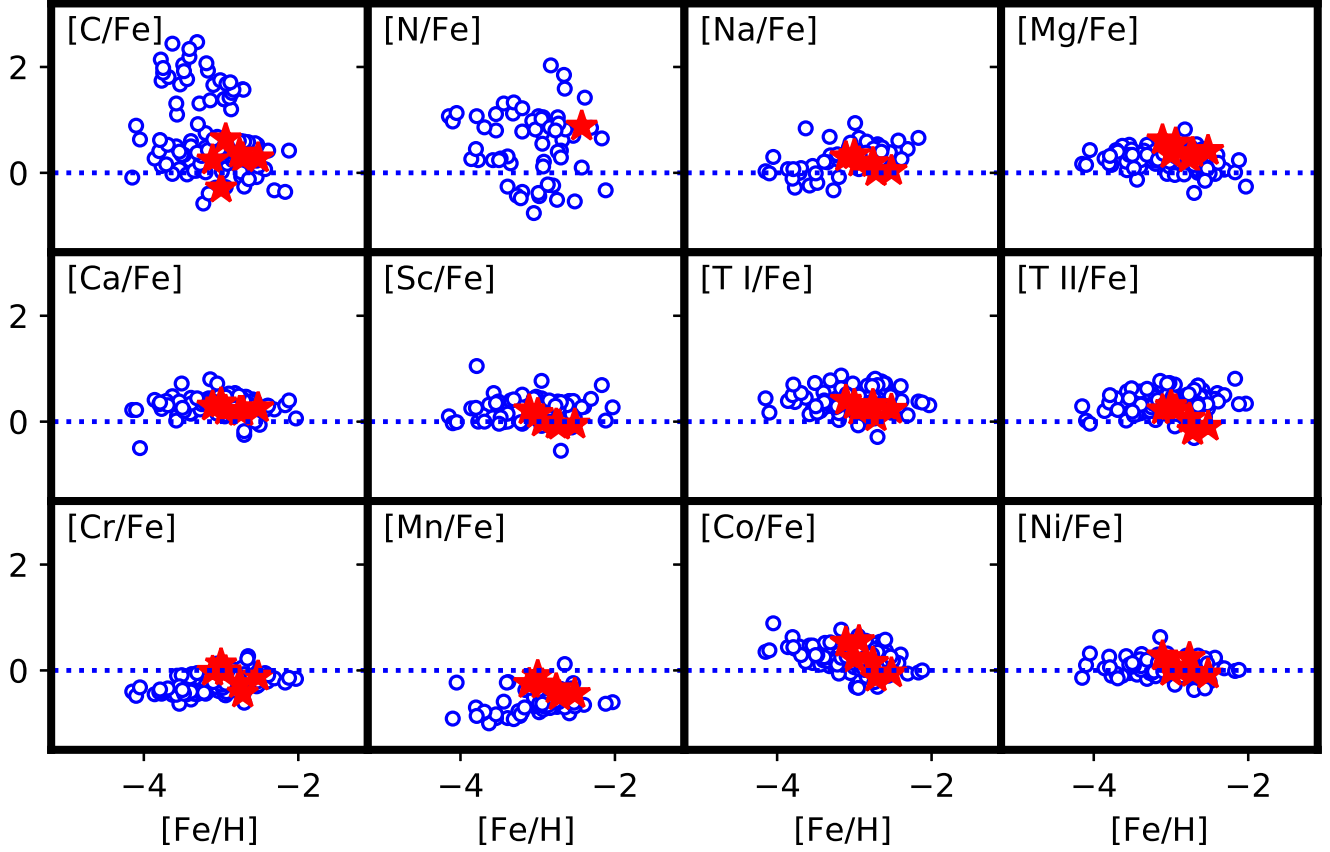


Figure 5. Selected light-elements abundances of our sample stars (red filled stars) overlaid with $[X/Fe]$ of carbon-normal metal-poor stars adopted from Yong et al. (2013) (blue open circles). Our derived $[X/Fe]$ show no significant differences compared to the literature data. $[C/Fe]$ values do not represent the carbon abundances of the natal gas.

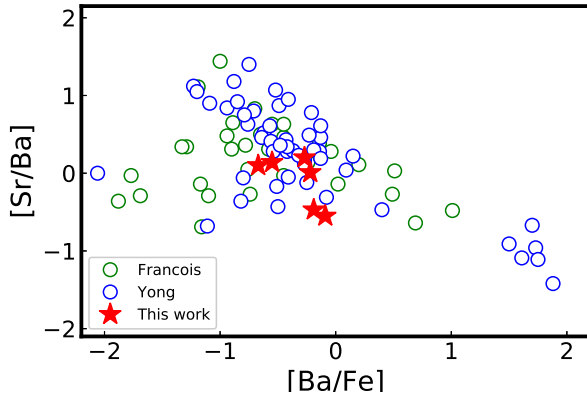


Figure 6. The determined abundance ratios $[Sr/Ba]$ of our sample stars (red filled stars), versus $[Ba/Fe]$. The green and blue open circles denote literature data adapted from François et al. (2007) and Yong et al. (2013), respectively.

s-process distributions for the rest of our sample stars. Heavier elements ($Z \geq 56$) in J0326+0202, J1256+3440,

J1413+1727, and J1630+0953 are in better agreement with the normalized SS r-process than the normalized SS s-process. The heavier elements in J2216+0246 seem to favor the normalized SS s-process. The abundance pattern in J1108+2530 is not in agreement with the SS abundance pattern.

Figure 8 shows the heavy element abundance patterns in our sample stars compared with abundance patterns of HD 122563 (the dashed gray line, Honda et al. 2006; Roederer et al. 2012), CS 22892052 (the solid red line, Sneden et al. 2003, 2009; Roederer et al. 2009), and predicted yields from s-process nucleosynthesis in TP-AGB stars (the dotted blue line, Sneden et al. 2008; Bisterzo et al. 2011). These patterns can be used as weak component of the r-process (HD 122563), main component of the r-process (CS 22892052), and main component of the s-process (TP-AGB yields) representatives (Roederer et al. 2014). The abundance pattern of HD122563 and CS 22892052 are renormalized to match the observed Eu, and the dotted blue line is renormalized to match the observed Ba.

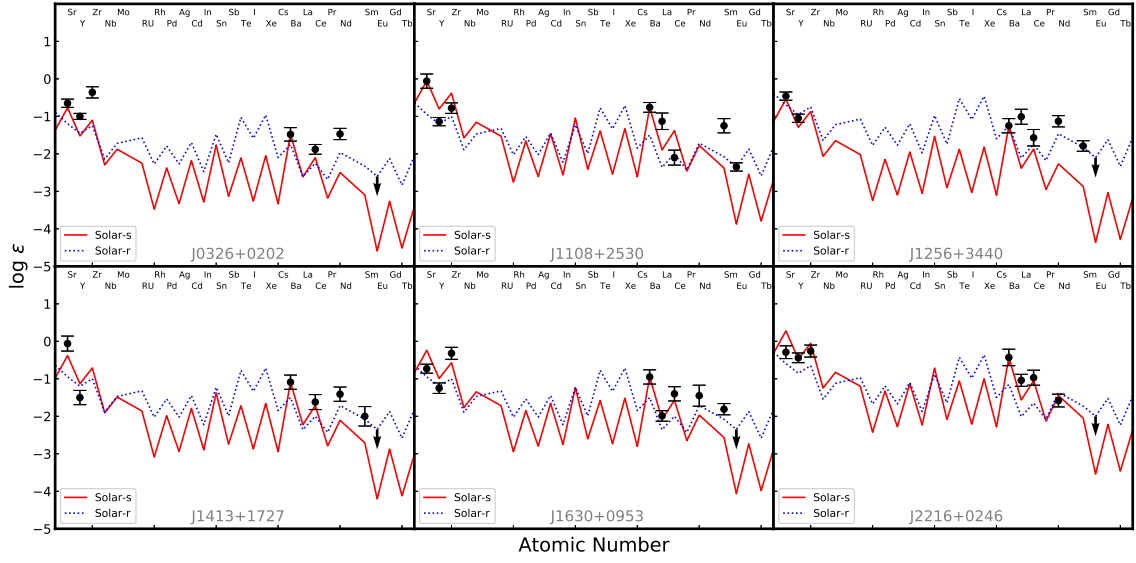


Figure 7. Elemental abundance patterns for the heavy element distribution in our sample stars (filled circles denote detections, and arrow denotes 3σ upper limits derived from Eu II line), compared with scaled solar system r- and s-process components adopted from [Burris et al. \(2000\)](#). The solar system r-process patterns are scaled to match Eu, and the solar system s-process patterns are scaled to match Ba.

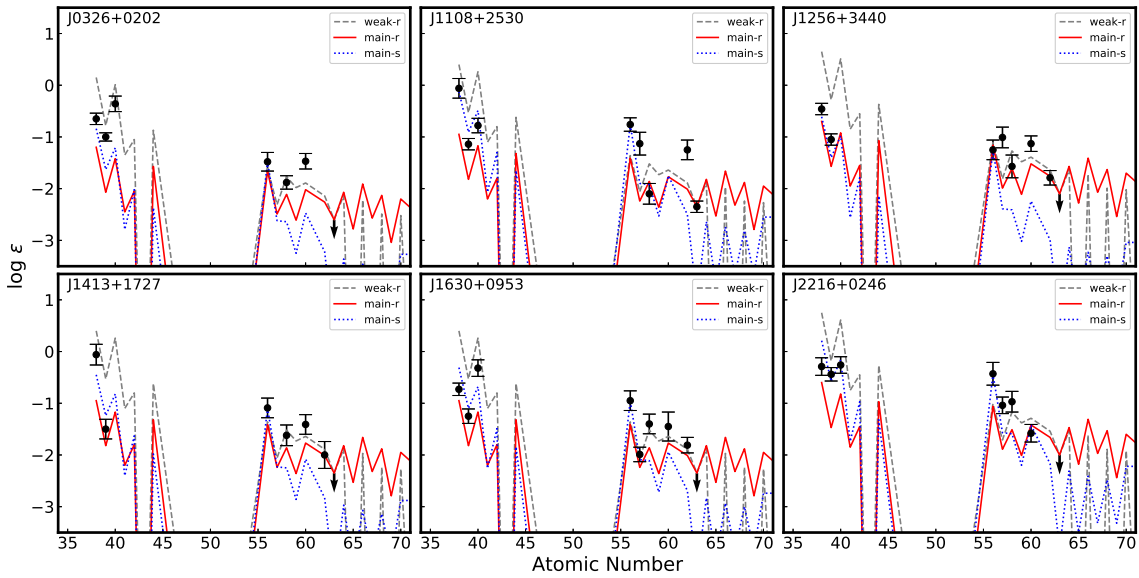


Figure 8. Neutron-capture element patterns in our sample stars. Filled circles denote detections, and arrow denotes 3σ upper limits derived from Eu II line. The dashed gray line denotes the observed abundances for the neutron-capture elements in HD122563 ([Honda et al. 2006](#); [Roederer et al. 2012](#)). The solid red line denotes the observed abundances for the neutron-capture elements in CS 22892052 ([Snedden et al. 2003, 2009](#); [Roederer et al. 2009](#)). The dotted blue line denotes predicted yields from s-process nucleosynthesis in TP-AGB stars ([Snedden et al. 2008](#); [Bisterzo et al. 2011](#)). The physical meaning of these three lines are discussed in the text.

The abundance patterns for the heavy elements ($Z \geq 56$)

observed in the sample stars are in better agreement

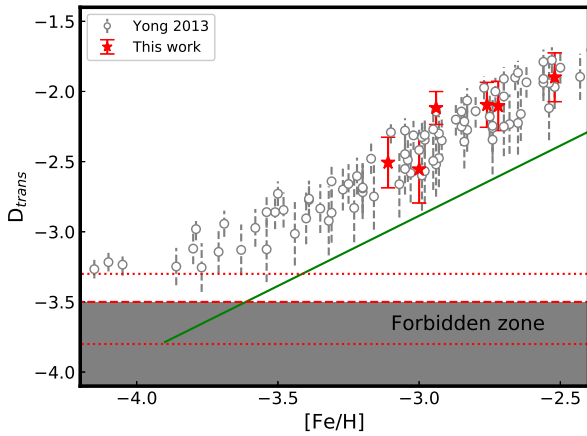


Figure 9. D_{trans} as a function of $[Fe/H]$ for our target stars, compared with Yong et al. (2013). The solid green line denotes the scaled solar pattern, the red dashed line denotes the limit of D_{trans} based on the model described in Frebel et al. (2007), and the red dotted lines show the uncertainty of the model. The shaded area is the Forbidden Zone, where there is insufficient C and O induced cooling for low-mass star formation.

with the weak component of the r-process (represented by HD 122563), with a partial s-process contribution in J1108+2530, J1630+0953, and J2216+0246.

In addition to the possible nucleosynthesis pathway(s) suggested above, it is now commonly acknowledged that the formation of Pop II low-mass stars requires additional coolants compared to the formation of Pop III massive stars (e.g., Yoshida et al. 2006; Glover 2013; Greif 2015). At present, a widely acceptable scenario tries to explain the transition from Pop III to Pop II stars by the notion of the fine-structure cooling of the C II and O I lines (e.g., Bromm & Loeb 2003; Santoro & Shull 2006). Therefore, C- and O-poor stars can place crucial constraints on the conditions under which metallicity of the ISM the Pop II stars may have been formed.

Frebel et al. (2007) suggested a criterion for the transition to Pop II (“transition discriminant” – $D_{trans} = -3.5$), which combines logarithmic abundance ratios of $[C/H]$ and $[O/H]$. Figure 9 shows the calculated D_{trans} for our sample stars and carbon-normal stars adopted from Yong et al. (2013). The green solid line denotes the solar D_{trans} values adopted from Asplund et al. (2009), the red dashed and the red dotted lines denote the limit of D_{trans} and its associated uncertainty, respectively, and the gray shaded area represents the Forbidden Zone. Even though the empirical formula of the D_{trans} requires both abundances ($[C/H]$ and $[O/H]$), it is possible to calculate D_{trans} where only one of these abundance ratios is known. Here we assume that $[O/Fe]$

$= 0.88 \pm 0.28$, following the linear relation between the $[C/O]$ and $[C/Fe]$ suggested by Cayrel et al. (2004). We can notice that our sample stars are located above the solar D_{trans} values and the Forbidden Zone, suggesting that they may have likely formed from a gas cloud exhibiting fine-structure cooling process.

5.2. J1630+0953 and J2216+0246 Possible Progenitors

Under the assumption that J1630+0953 and J2216+0246 are CEMP-no stars, we decided to gain insights into their putative progenitors, by comparing their abundance patterns with theoretical predictions from Heger & Woosley (2010). For the convenience of the reader, it is worth mentioning that this grid does not consider rotation and has a χ^2 matching algorithm over 16,800 models. The parameter space includes progenitor masses ($10\text{--}100 M_{\odot}$), explosion energies ($0.3\text{--}10 \times 10^{51}$ erg), and mixing factor (f_{mix}) ranging from no mixing to nearly complete mixing (see Heger & Woosley 2010, for more information).

We sampled 10^4 sets of the determined chemical abundances of J1630+0953 and J2216+0246, assuming a normal distribution. To facilitate this exercise, we use the determined $\log \epsilon(X)$ of J1630+0953 and J2216+0246 as the central values and dispersions given by the associated uncertainties (see references to Table 4). This allowed us to generate 10^4 abundance patterns for each star. We use the publicly available STARFIT code (Heger & Woosley 2010) to find the progenitor mass and explosion energy for the 10^4 abundance patterns. Figure 10 shows the determined abundances of J1630+0953 and J2216+0246 (black filled circles), with error bars representing their associated uncertainties, overlaid with abundance patterns generated by several best fit models. Figure 11 shows posterior distributions for the mean squared residuals of the 10^4 fittings, for both stars. Legends show the median value and the median absolute deviation (MAD). The MAD can be used as a robust estimator on how the data spreads out. In other words, the larger the MAD, the greater the variability in χ^2 .

For J1630+0953, an SN model with mass $21.5 M_{\odot}$ and explosion energy 0.3×10^{51} erg was the most frequent model (92 %) to fit the generated abundance patterns. Another model with mass $50.0 M_{\odot}$ and explosion energy 10.0×10^{51} erg fit 6 % of the generated abundance patterns, while the remaining of the 10^4 generated abundance patterns (249) had best fit models with mass $25.0 M_{\odot}$ and explosion energy 0.3×10^{51} erg.

For J2216+0246, a larger number of SN models were able to fit our 10^4 generated abundance patterns. About 45 % (4532) of the generated abundance patterns had

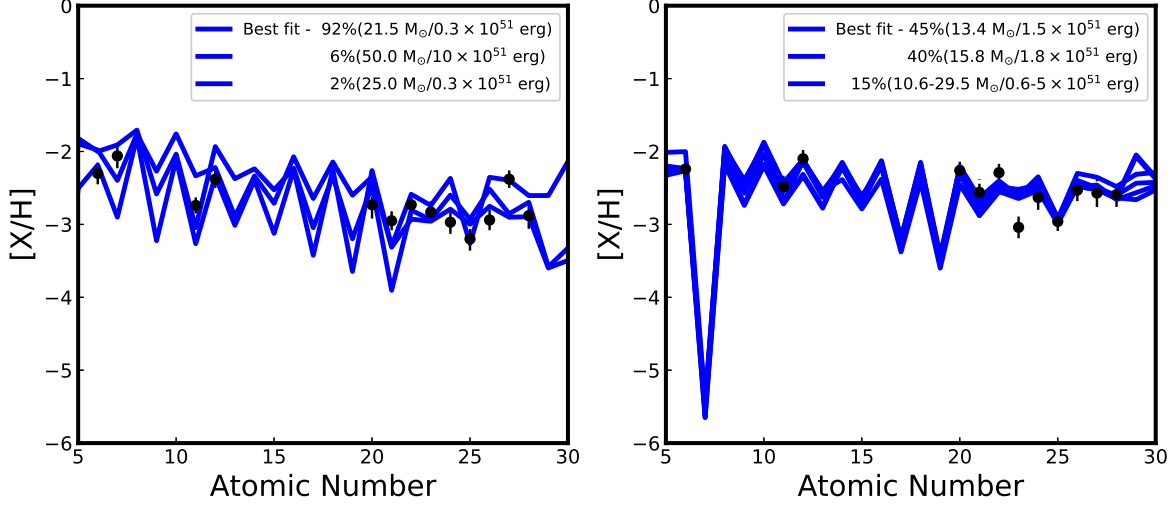


Figure 10. The determined $[X/H]$ abundance ratios of J1630+0953 (left panel) and J2216+0246 (right panel) as a function of atomic number, overlaid with simulated abundance patterns by several best fit models, transparent by their fractional appearance. The best fits and their properties are discussed in the text.

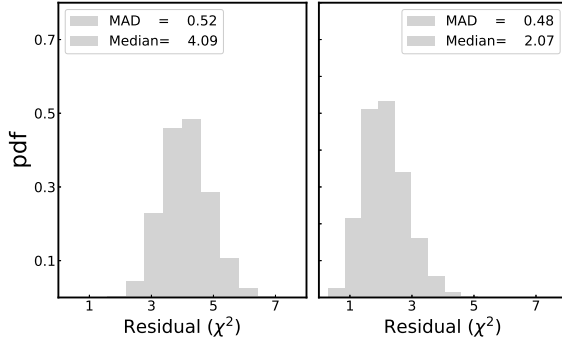


Figure 11. Posterior Distributions for χ^2 , of the 10,000 simulations, for J1630+0953 (left panel) and J2216+0246 (right panel). The median and median absolute deviation (MAD) are shown in legends.

best fit with an SN model with mass of $13.4 M_{\odot}$ and explosion energy of 1.5×10^{51} erg. Another SN model with mass $15.8 M_{\odot}$ and explosion energy 1.8×10^{51} erg was the best fit of 40 % (3976) of the generated abundance patterns; while 21 different SN models correspond to the best fit for the rest of the 10^4 generated abundance patterns (1492). In total, 23 different SN models were the best fits for the 10^4 generated abundance patterns of J2216+0246, in the mass range $10.6\text{--}29.5 M_{\odot}$ and explosion energies $0.6\text{--}5 \times 10^{51}$ erg. The abundance patterns simulated by these 23 models are shown in the right panel of Figure 10, and color-coded by their fractional appearance.

Regarding the most frequent SN model in the exercise of J1630+0953, it can be seen through either visual checking or χ^2 , that the carbon ($Z=6$) and nitrogen ($Z=7$) abundances are well reproduced (within $\sim 2 \sigma$). Sodium ($Z=11$) is overproduced, while magnesium ($Z=12$) is well reproduced (within $\sim 1 \sigma$). Elements from calcium to iron ($Z=20\text{--}26$) are also well reproduced (within $\sim 2 \sigma$). The cobalt ($Z=27$) abundance is underproduced, which is not unusual for theoretical models, where an SN model with higher mass, explosion energy, and mixing factor may result better Co fitting, although this could worsen other elements fittings (see Tominaga et al. 2014, and references therein), while the Nickel ($Z=28$) is well reproduced. The predicted yields in $\sim 85\%$ of the SN models reproduced the observed abundances for J2216+0246 within $\sim 2 \sigma$.

In general, J1630+0953 has possible progenitor with $21\text{--}25 M_{\odot}$ stellar mass and explosion energy 0.3×10^{51} erg, while the mass and explosion energy of the possible progenitors of J2216+0246 are somewhat lower ($10.6\text{--}29.5 M_{\odot}$, $0.6\text{--}5 \times 10^{51}$ erg). Recently, Ishigaki et al. (2018) compared the abundance patterns of 219 EMP stars with supernova yields of metal-free stars to find that the best fitting progenitor SNe of most EMP stars are Pop III stars in the range $15\text{--}25 M_{\odot}$. **The analysis presented in this paper supports this hypothesis and suggests that the peak around $20 M_{\odot}$ may reflect the Pop III initial mass function and more massive SN might be more energetic than their ejecta escape from the halo and would never be incorporated into the next generation of stars.**

5.3. Kinematics and Dynamics

The full space motion of our sample stars can be derived by combining positions (α , δ), proper motions ($\mu_\alpha \cos \delta$, μ_δ), available in Gaia DR2 (Gaia Collaboration et al. 2018), the line-of-sight velocities (V_r), derived from our high-resolution spectra (see Section 2.1), and a Galactic potential model. Errors are provided in Gaia DR2, thus the inversion of the parallax (ϖ) to calculate the stellar distance is not appropriate (see Luri et al. 2018, for a recent discussion). Therefore, we adopted distances from Bailer-Jones et al. (2018), who inferred distances to all stars, with published parallaxes, in Gaia DR2 using a weak distance prior. Gaia DR2 ID source, positions, proper motions, distances, and the associated uncertainties for these quantities, are listed in Table 6.

We sampled 10^4 sets of the observed astrometric quantities (RA, DEC, ϖ , RV, $\mu_\alpha \cos \delta$, μ_δ) from the measurement errors of each quantity for each star in our sample (see references to Table 6). We assume that the Sun has an offset above the Galactic midplane of $z_\odot = 25$ pc (Jurić et al. 2008), $R_\odot = 8.2$ kpc (Bland-Hawthorn & Gerhard 2016) as the distance from the Galactic center, circular velocity $v_0 = 232.8$ km s $^{-1}$ at the Solar position (McMillan 2017), and solar peculiar motion $(U_\odot, V_\odot, W_\odot) = (11.1, 12.24, 7.25)$ km s $^{-1}$ (Bland-Hawthorn & Gerhard 2016). We calculate the Galactocentric Cartesian (X_{GC}, Y_{GC}, Z_{GC}) coordinates as follows:

$$\begin{aligned} X_{GC} &= R_\odot - d \cos(b) \cos(\ell) \\ Y_{GC} &= -d \cos(b) \sin(\ell) \\ Z_{GC} &= d \sin(b) + z_\odot \end{aligned}$$

We calculated and corrected the Galactic space-velocity components (U, V, W) using the Astropy Galactocentric frame package (Astropy Collaboration et al. 2013, 2018): U (positive toward the Galactic center), V (positive in the direction of Galactic rotation) and W (positive toward the North Galactic Pole). Moreover, we define the angle $\phi = \tan^{-1}(Y_{GC}/X_{GC})$ and then calculate the cylindrical velocities components for our sample as follows:

$$\begin{aligned} V_R &= U \cos(\phi) + V \sin(\phi) \\ V_\phi &= U \sin(\phi) - V \cos(\phi) \\ V_z &= W \end{aligned}$$

We adopted the MWPotential2014 as a Galactic potential model (see Bovy 2015, for more information)

to integrate the corresponding stellar orbits, apocentric (r_{apo}) and pericentric (r_{peri}) radii, the maximum offset from the Galactic midplane (Z_{max}), and eccentricity, defined as $e = (r_{\text{apo}} - r_{\text{peri}})/(r_{\text{apo}} + r_{\text{peri}})$. In addition, we derived the total orbital energy, defined as $E = (1/2)v^2 + \Phi(\mathbf{x})$ and the angular momentum in the vertical direction, defined as $L_z = R \times V_\phi$, where R denotes the distance from the Galactic center projected onto the disk plane.

Table 7 lists, for each star in our sample, the calculated median for the Galactic positions (X_{GC}, Y_{GC}, Z_{GC}), Galactic velocities (U, V, W, V_R , and V_ϕ), as well as V_\perp , defined as $(V_R^2 + V_z^2)^{1/2}$. Table 8 lists the calculated median for the orbital parameters, energy and angular momentum. We also provide an estimated $\sim 1 \sigma$ uncertainty of each quantity in our calculations, defined as the differences between the median and 84th percentiles (superscript), and the differences between the median and 16th percentiles (subscript).

Figure 12 shows the behavior of the calculated velocities and orbital properties, for our sample stars, as a function of [Fe/H]. Error bars denote typical [Fe/H] uncertainty (x-axis) and the 16th and 84th percentiles (y-axis). It is possible to see that 66 % of our sample is moving away ($V_R > 0$) from the Galactic center, 100% on prograde ($V_\phi > 0$) orbits, and 50 % moving north ($V_z > 0$), as they pass through the Galactic disk. The right panel shows that only J1108+2530 and J1256+3440 have $r_{\text{apo}} > 15.0$ kpc and $e > 0.7$ and the majority of our sample stars pass the Galactic center at $r_{\text{peri}} = 4.16$. Also, 66% of our sample stars travel at least 7 kpc above or below the Galactic plane.

An additional tool that can be used for this analysis is the Lindblad diagram. By plotting the total orbital energy vs. angular momentum in the vertical direction, one can assess the accretion origin of the sample stars. Carollo et al. (2014) explored kinematics, integrals of motion, and orbital properties of 323 VMP stars, to establish a method to assign membership to the inner- and outer-halo populations. In this context, stars with total energy > -0.9 km 2 s $^{-2}$ and $r_{\text{apo}} > 15$ kpc can be considered as outer-halo stars. Otherwise, stars can be considered as members of the inner-halo population.

Figure 13 shows the Lindblad diagram (top panel) and the Carollo et al. (2014) criterion (bottom panel) for the sample stars, compared to stars taken from Paper I. CEMP-no stars are shown as blue filled stars, CEMP-r/s star as orange filled square, and C-normal stars as black filled stars. The green dashed curve represents the locus of the points that possess constant apo-Galactic radius, $r_{\text{apo}} = 15$ kpc. The light-gray shaded area encloses the transition zone energies. It is possible to see that

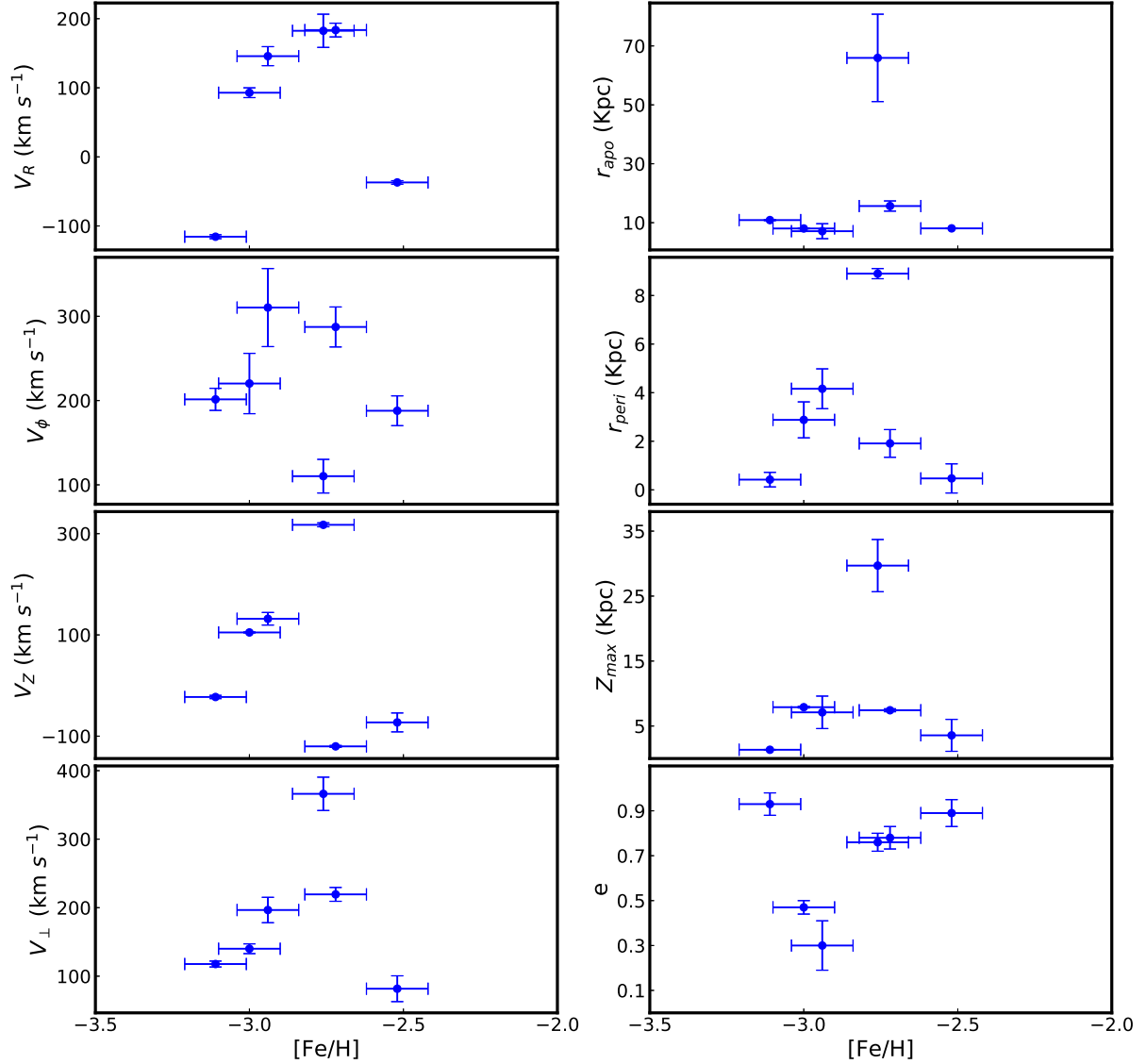


Figure 12. The left panel shows the Galactic velocities and the right panel shows the orbital parameters for our sample stars as functions of $[\text{Fe}/\text{H}]$. The y-axis error bars denote the 16th and 84th percentiles, while the x-axis error bars represent a typical $[\text{Fe}/\text{H}]$ uncertainty (0.10 dex).

J1630+0953 and J2216+0246, within the error bars, are likely to have inner-halo kinematics.

Many numerical cosmological simulations suggest that the main origin of the Milky Way inner and outer-halo stars are massive and low-mass subgalactic fragments, respectively (Zolotov et al. 2009; Font et al. 2011; McCarthy et al. 2012; Beers et al. 2012; Tissera et al. 2013,

2014). In general, We can understand the origin of our stars by examining a combination of their orbital parameters and integrals of motion. The derived orbital parameters and the calculated total energy of J1630+0953 and J2216+0246 suggest that they probably belong to the inner-halo population. **However, their metallicity and C-enhancement indicate that they may**

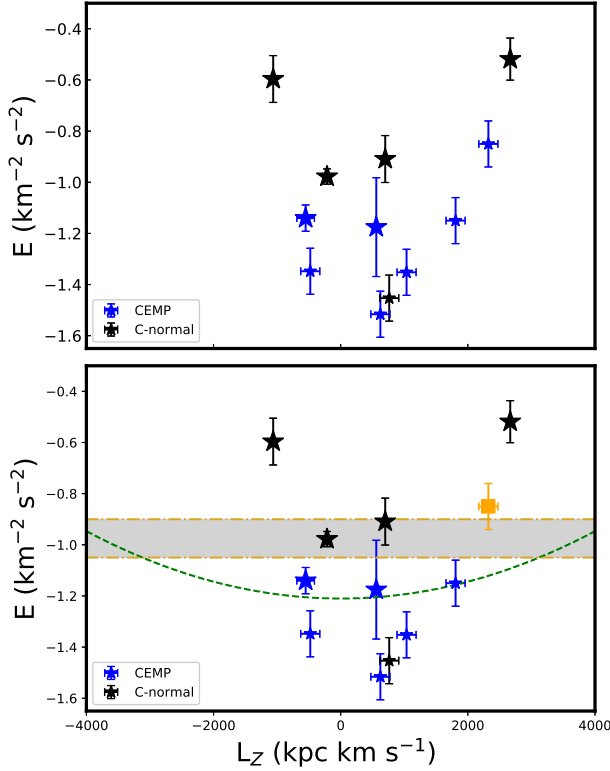


Figure 13. Lindblad diagram for program stars and data taken from Paper I. Top panel shows the distribution of this sample based on $[\text{C}/\text{Fe}]$ abundance ratios, carbon normal (black stars) and CEMP stars (red stars). Bottom panel shows the distribution of this sample based on Carollo et al. (2014) criterion. CEMP-no stars are shown as blue filled star, CEMP-r/s as orange filled square, and C-normal stars as black filled star. The green dashed curve represents the locus of the points that possess constant apo-Galactic radius, $\text{rapo} = 15$ kpc. The light-gray shaded area encloses the transition zone energies.

have formed not in situ but in small mass sub-galactic fragments that were accreted very early on and contributed to the old central regions of the halo system (e.g., Tissera et al. 2018).

6. CONCLUSIONS

In this paper, we analyzed six metal-poor stars chosen from the LAMOST database and followed-up, for the first time, with high-resolution observations using Lick/APF. We have presented stellar parameters and full detail chemical abundances (23 individual elements from C to Eu), for these stars. Our analysis shows no significant differences compared with the general abun-

dance trends as reported in previous studies of metal-poor stars. In particular, J1630+0953 and J2216+0246 present a different behavior ($[\text{C}/\text{Fe}] \geq +0.7$ and $[\text{Ba}/\text{Fe}] < 0.0$) and are classified as new members of the CEMP-no class.

We have attempted to characterize the formation scenario and the progenitors of our CEMP-no stars. Our program stars are located above the solar D_{trans} values and the Forbidden Zone, suggesting that they may have likely formed from a gas cloud exhibiting fine-structure cooling process. Furthermore, we have compared 10^4 generated sets of the determined chemical abundances of the light-element abundances of J1630+0953 and J2216+0246 with predicted yields from nonrotating massive-star models. About $\sim 94\%$ of the models predicted that the mass and explosion energy of the J1630+0953 progenitor, could be in the $21\text{-}25 M_{\odot}$ mass range and 0.3×10^{51} erg, respectively, and only about $\sim 6\%$ with mass of $50 M_{\odot}$ and explosion energy of 10.0×10^{51} erg. In about $\sim 85\%$ of the models predicted $13\text{-}16 M_{\odot}$ mass range and explosion energy of $1.5\text{-}1.8 \times 10^{51}$ erg for the progenitor of J2216+0246, while the remaining models ($\sim 15\%$) predicted $10.6\text{-}29.5 M_{\odot}$ mass range and explosion energy $0.6\text{-}5 \times 10^{51}$ erg. In general, our comparison suggested that massive stellar progenitors shall be the pollutant source of their birth cloud, and these pollutants then acted as cooling agents. Our result is consistent with recent conclusions given by Ishigaki et al. (2018), which suggest possible progenitors in the $15\text{-}25 M_{\odot}$ mass range. **This peak ($\sim 20 M_{\odot}$) may reflect the PopIII initial mass function. However, this brings the possibility as to whether more massive SN might be more energetic and therefore destroy their host halo and not allow for EMP star formation afterwards.**

We have further investigated the kinematics and dynamics of the sample stars, based on Gaia DR2 data. Our results show that all stars are members of the inner-halo population. Nevertheless, the deficiency in iron and enhancement in carbon abundances of J1630+0953 and J2216+0246 strongly suggest that these stars were born in low-mass sub-galactic systems and later accreted during the initial phases of Galaxy assembly and contributed to the old stellar populations of the inner halo.

ACKNOWLEDGEMENT

We thank the anonymous referee for a prompt and constructive report. M. K. M. thanks The World Academy of Sciences and the Chinese Academy of Sciences for the CAS-TWAS fellowship. M. K. M. thanks Ian Roederer and Tilman Hartwig for valuable discussions and helpful comments on earlier versions of the

manuscript. M. K. M. thanks Monika Adamów for her help with using pyMOOGi code. This study is supported by the National Natural Sciences Foundation of China under grant No. 11890694 and 11573032. V.M. P. acknowledges partial support for this work from grant PHY 1430152; Physics Frontier Center/JINA Center for

the Evolution of the Elements (JINA-CEE), awarded by the US National Science Foundation (NSF).

Software: IRAF (Tody 1986, 1993), TAME (Kang & Lee 2015), MOOG (Snedden 1973; Sobeck et al. 2011; Adamow 2017), STARFIT (Heger & Woosley 2010), R-project (R Core Team 2018), NumPy (van der Walt et al. 2011), SciPy (Jones et al. 2001–), Matplotlib (Hunter 2007), Astropy (Astropy Collaboration et al. 2013, 2018).

REFERENCES

- Adamow, M. M. 2017, in American Astronomical Society Meeting Abstracts, Vol. 230, American Astronomical Society Meeting Abstracts #230, 216.07
- Alonso, A., Arribas, S., & Martínez-Roger, C. 1999, A&AS, 140, 261
- Andrievsky, S. M., Spite, F., Korotin, S. A., et al. 2011, A&A, 530, A105
- Aoki, W., Beers, T. C., Christlieb, N., et al. 2007, ApJ, 655, 492
- Aoki, W., Suda, T., Boyd, R. N., Kajino, T., & Famiano, M. A. 2013a, ApJL, 766, L13
- Aoki, W., Frebel, A., Christlieb, N., et al. 2006, ApJ, 639, 897
- Aoki, W., Beers, T. C., Lee, Y. S., et al. 2013b, AJ, 145, 13
- Asplund, M., Grevesse, N., Sauval, A. J., & Scott, P. 2009, ARA&A, 47, 481
- Astropy Collaboration, Robitaille, T. P., Tollerud, E. J., et al. 2013, A&A, 558, A33
- Astropy Collaboration, Price-Whelan, A. M., Sipőcz, B. M., et al. 2018, AJ, 156, 123
- Bailer-Jones, C. A. L., Rybizki, J., Foesneau, M., Mantelet, G., & Andrae, R. 2018, AJ, 156, 58
- Beers, T. C., Carollo, D., Lee, Y., Kennedy, C. R., & SEGUE Collaboration. 2012, in American Astronomical Society Meeting Abstracts, Vol. 219, American Astronomical Society Meeting Abstracts #219, 222.06
- Beers, T. C., & Christlieb, N. 2005, ARA&A, 43, 531
- Beers, T. C., Placco, V. M., Carollo, D., et al. 2017, ApJ, 835, 81
- Bisterzo, S., Gallino, R., Straniero, O., Cristallo, S., & Käppeler, F. 2011, MNRAS, 418, 284
- Bland-Hawthorn, J., & Gerhard, O. 2016, ARA&A, 54, 529
- Bovy, J. 2015, ApJS, 216, 29
- Bromm, V., & Loeb, A. 2003, Nature, 425, 812
- Burris, D. L., Pilachowski, C. A., Armandroff, T. E., et al. 2000, ApJ, 544, 302
- Caffau, E., Gallagher, A. J., Bonifacio, P., et al. 2018, A&A, 614, A68
- Caffau, E., Bonifacio, P., François, P., et al. 2011, Nature, 477, 67
- Carollo, D., Freeman, K., Beers, T. C., et al. 2014, ApJ, 788, 180
- Casagrande, L., Ramírez, I., Meléndez, J., Bessell, M., & Asplund, M. 2010, A&A, 512, A54
- Casagrande, L., & VandenBerg, D. A. 2014, MNRAS, 444, 392
- . 2018a, MNRAS, 479, L102
- . 2018b, MNRAS, 475, 5023
- Castelli, F., & Kurucz, R. L. 2003, in IAU Symposium, Vol. 210, Modelling of Stellar Atmospheres, ed. N. Piskunov, W. W. Weiss, & D. F. Gray, A20
- Cayrel, R., Depagne, E., Spite, M., et al. 2004, A&A, 416, 1117
- Charbonnel, C. 1994, A&A, 282, 811
- Christlieb, N., Bessell, M. S., Beers, T. C., et al. 2002, Nature, 419, 904
- Cohen, J. G., Christlieb, N., McWilliam, A., et al. 2008, ApJ, 672, 320
- Cristallo, S., Straniero, O., Gallino, R., et al. 2009, ApJ, 696, 797
- Cristallo, S., Piersanti, L., Straniero, O., et al. 2011, ApJS, 197, 17
- Cruz, M. A., Cogo-Moreira, H., & Rossi, S. 2018, MNRAS, 475, 4781
- Cui, X.-Q., Zhao, Y.-H., Chu, Y.-Q., et al. 2012, Research in Astronomy and Astrophysics, 12, 1197
- Demarque, P., Woo, J.-H., Kim, Y.-C., & Yi, S. K. 2004, ApJS, 155, 667
- Ezzeddine, R., Frebel, A., Roederer, I. U., et al. 2019, arXiv e-prints, arXiv:1904.03211
- Font, A. S., McCarthy, I. G., Crain, R. A., et al. 2011, MNRAS, 416, 2802
- François, P., Depagne, E., Hill, V., et al. 2007, A&A, 476, 935
- Frebel, A. 2018, Annual Review of Nuclear and Particle Science, 68, 237

- Frebel, A., Casey, A. R., Jacobson, H. R., & Yu, Q. 2013, *ApJ*, 769, 57
- Frebel, A., Johnson, J. L., & Bromm, V. 2007, *MNRAS*, 380, L40
- Frebel, A., Aoki, W., Christlieb, N., et al. 2005, *Nature*, 434, 871
- Frischknecht, U., Hirschi, R., & Thielemann, F.-K. 2012, *A&A*, 538, L2
- Gaia Collaboration, Brown, A. G. A., Vallenari, A., et al. 2018, *A&A*, 616, A1
- Glover, S. 2013, in *Astrophysics and Space Science Library*, Vol. 396, *The First Galaxies*, ed. T. Wiklind, B. Mobasher, & V. Bromm, 103
- Greif, T. H. 2015, *Computational Astrophysics and Cosmology*, 2, 3
- Grillmair, C. J. 2009, *ApJ*, 693, 1118
- Hansen, C. J., Montes, F., & Arcones, A. 2014, *ApJ*, 797, 123
- Hansen, C. J., Nordström, B., Hansen, T. T., et al. 2016a, *A&A*, 588, A37
- Hansen, T. T., Andersen, J., Nordström, B., et al. 2016b, *A&A*, 586, A160
- . 2016c, *A&A*, 588, A3
- Heger, A., & Woosley, S. E. 2010, *ApJ*, 724, 341
- Helmi, A., Babusiaux, C., Koppelman, H. H., et al. 2018, *Nature*, 563, 85
- Hirschi, R. 2007, *A&A*, 461, 571
- Hollek, J. K., Frebel, A., Roederer, I. U., et al. 2011, *ApJ*, 742, 54
- Honda, S., Aoki, W., Ishimaru, Y., Wanajo, S., & Ryan, S. G. 2006, *ApJ*, 643, 1180
- Hunter, J. D. 2007, *Computing In Science & Engineering*, 9, 90
- Iben, Jr., I. 1965, *ApJ*, 142, 1447
- Ishigaki, M. N., Tominaga, N., Kobayashi, C., & Nomoto, K. 2018, *ApJ*, 857, 46
- Ito, H., Aoki, W., Beers, T. C., et al. 2013, *ApJ*, 773, 33
- Jones, E., Oliphant, T., Peterson, P., et al. 2001–, *SciPy: Open source scientific tools for Python*, , [Online; accessed {today}]
- Jurić, M., Ivezić, Ž., Brooks, A., et al. 2008, *ApJ*, 673, 864
- Kang, W., & Lee, S.-G. 2015, *TAME: Tool for Automatic Measurement of Equivalent-width*, *Astrophysics Source Code Library*, , ascl:1503.003
- Keller, S. C., Bessell, M. S., Frebel, A., et al. 2014, *Nature*, 506, 463
- Lucatello, S., Tsangarides, S., Beers, T. C., et al. 2005, *ApJ*, 625, 825
- Lugaro, M., Karakas, A. I., Stancliffe, R. J., & Rijs, C. 2012, *ApJ*, 747, 2
- Luri, X., Brown, A. G. A., Sarro, L. M., et al. 2018, *A&A*, 616, A9
- Maeder, A., Meynet, G., & Chiappini, C. 2015, *A&A*, 576, A56
- Magain, P., & Zhao, G. 1996, *A&A*, 305, 245
- Mardini, M. K., Li, H., Placco, V. M., et al. 2019, *The Astrophysical Journal*, 875, 89
- Mashonkina, L., Jablonka, P., Pakhomov, Y., Sitnova, T., & North, P. 2017, *A&A*, 604, A129
- McCarthy, I. G., Font, A. S., Crain, R. A., et al. 2012, *MNRAS*, 420, 2245
- McMillan, P. J. 2017, *MNRAS*, 465, 76
- Meynet, G., Ekström, S., & Maeder, A. 2006, *A&A*, 447, 623
- Nomoto, K., Kobayashi, C., & Tominaga, N. 2013, *ARA&A*, 51, 457
- Placco, V. M., Beers, T. C., Reggiani, H., & Meléndez, J. 2016, *ApJL*, 829, L24
- Placco, V. M., Frebel, A., Beers, T. C., & Stancliffe, R. J. 2014a, *ApJ*, 797, 21
- Placco, V. M., Beers, T. C., Roederer, I. U., et al. 2014b, *ApJ*, 790, 34
- Qian, Y.-Z., & Wasserburg, G. J. 2003, *ApJ*, 588, 1099
- . 2008, *ApJ*, 687, 272
- R Core Team. 2018, *R: A Language and Environment for Statistical Computing*, R Foundation for Statistical Computing, Vienna, Austria
- Ramírez, I., & Meléndez, J. 2005, *ApJ*, 626, 465
- Roederer, I. U., Kratz, K.-L., Frebel, A., et al. 2009, *ApJ*, 698, 1963
- Roederer, I. U., Preston, G. W., Thompson, I. B., Shectman, S. A., & Sneden, C. 2014, *ApJ*, 784, 158
- Roederer, I. U., Lawler, J. E., Sobeck, J. S., et al. 2012, *ApJS*, 203, 27
- Santoro, F., & Shull, J. M. 2006, *ApJ*, 643, 26
- Schlegel, D. J., Finkbeiner, D. P., & Davis, M. 1998, *ApJ*, 500, 525
- Skrutskie, M. F., Cutri, R. M., Stiening, R., et al. 2006, *AJ*, 131, 1163
- Sneden, C., Cowan, J. J., & Gallino, R. 2008, *ARA&A*, 46, 241
- Sneden, C., Lawler, J. E., Cowan, J. J., Ivans, I. I., & Den Hartog, E. A. 2009, *ApJS*, 182, 80
- Sneden, C., Cowan, J. J., Lawler, J. E., et al. 2003, *ApJ*, 591, 936
- Sneden, C. A. 1973, PhD thesis, THE UNIVERSITY OF TEXAS AT AUSTIN.
- Sobeck, J. S., Kraft, R. P., Sneden, C., et al. 2011, *AJ*, 141, 175

- Starkenburg, E., Shetrone, M. D., McConnachie, A. W., & Venn, K. A. 2014, *MNRAS*, 441, 1217
- Starkenburg, E., Aguado, D. S., Bonifacio, P., et al. 2018, *MNRAS*, 481, 3838
- Thielemann, F.-K., Eichler, M., Panov, I. V., & Wehmeyer, B. 2017, *Annual Review of Nuclear and Particle Science*, 67, 253
- Tissera, P. B., Beers, T. C., Carollo, D., & Scannapieco, C. 2014, *MNRAS*, 439, 3128
- Tissera, P. B., Machado, R. E. G., Carollo, D., et al. 2018, *MNRAS*, 473, 1656
- Tissera, P. B., Scannapieco, C., Beers, T. C., & Carollo, D. 2013, *MNRAS*, 432, 3391
- Tody, D. 1986, in *Proc. SPIE*, Vol. 627, *Instrumentation in astronomy VI*, ed. D. L. Crawford, 733
- Tody, D. 1993, in *Astronomical Society of the Pacific Conference Series*, Vol. 52, *Astronomical Data Analysis Software and Systems II*, ed. R. J. Hanisch, R. J. V. Brissenden, & J. Barnes, 173
- Tominaga, N., Iwamoto, N., & Nomoto, K. 2014, *ApJ*, 785, 98
- Tominaga, N., Umeda, H., & Nomoto, K. 2007, *ApJ*, 660, 516
- Umeda, H., & Nomoto, K. 2003, *Nature*, 422, 871
- van der Walt, S., Colbert, S. C., & Varoquaux, G. 2011, *Computing in Science and Engineering*, 13, 22
- Vogt, S. S., Radovan, M., Kibrick, R., et al. 2014, *PASP*, 126, 359
- Yong, D., Norris, J. E., Bessell, M. S., et al. 2013, *ApJ*, 762, 26
- Yoon, J., Beers, T. C., Placco, V. M., et al. 2016, *ApJ*, 833, 20
- Yoon, J., Beers, T. C., Dietz, S., et al. 2018, *ApJ*, 861, 146
- Yoshida, N., Omukai, K., Hernquist, L., & Abel, T. 2006, *ApJ*, 652, 6
- Zacharias, N., Finch, C. T., Girard, T. M., et al. 2013, *AJ*, 145, 44
- Zhao, G., Chen, Y.-Q., Shi, J.-R., et al. 2006, *ChJA&A*, 6, 265
- Zhao, G., Zhao, Y.-H., Chu, Y.-Q., Jing, Y.-P., & Deng, L.-C. 2012, *Research in Astronomy and Astrophysics*, 12, 723
- Zolotov, A., Willman, B., Brooks, A. M., et al. 2009, *ApJ*, 702, 1058

Table 1. Log of the Lick/APF Observations

	ID	Date	RA	DEC	r	Exptime	S/N	V_r
					(mag)	(s)	(pixel ⁻¹)	(km s ⁻¹)
1	J0326+0202	18 Nov 2015	03 26 53.88	+02 02 28.1	11.55	1800*4	45	116.2
2	J1108+2530	16 Mar 2015	11 08 47.18	+25 30 47.2	12.16	1800*4	32	-114.62
3	J1256+3440	30 May 2015	12 56 42.41	+34 40 58.9	12.64	1800*4	30	284.06
4	J1413+1727	24 Jun 2015	14 13 15.67	+17 27 20.8	11.85	1800*4	42	106.18
5	J1630+0953	23 Jun 2015	16 30 35.82	+09 53 17.0	12.98	1800*4	30	57.82
6	J2216+0246	24 Jun 2015	22 16 35.96	+02 46 17.0	12.47	1800*4	32	-94.88

NOTE—The S/N ratio per pixel was measured using IRAF at $\lambda \sim 4500 \text{ \AA}$.

Table 2. Equivalent Widths of Our Sample.

λ	Species	χ	$\log gf$	J0326+0202	J1108+2530	J1256+3440	J1413+1727	J1630+0953	J2216+0246
(Å)		eV		mÅ	mÅ	mÅ	mÅ	mÅ	mÅ
4312	C(CH)	—	—	syn	syn	syn	syn	syn	syn
4323	C(CH)	—	—	syn	syn	syn	syn	syn	syn
4214	N(CN)	—	—	syn	syn	syn	syn	syn	syn
5889.95	Na I	0.00	0.10	99.5	132.5	146.6	158.0	144.0	142.3
5895.92	Na I	0.00	-0.20	122.0	115.2	58.3	125.0	136.3	110.4
4057.50	Mg I	4.35	-0.89	45.9	31.6	24.0	—	—	26.0
4167.27	Mg I	4.35	-0.71	32.7	31.5	45.4	—	33.3	59.0
4571.10	Mg I	0.00	-5.69	22.4	46.3	—	34.3	55.8	68.6
4702.99	Mg I	4.33	-0.44	44.5	57.2	24.1	53.7	73.4	76.7
5172.68	Mg I	2.71	-0.45	—	—	—	168.1	—	—
5183.60	Mg I	2.72	-0.24	—	—	—	178.8	—	—
5528.40	Mg I	4.35	-0.50	42.7	60.2	41.3	48.3	58.9	88.4
4283.01	Ca I	1.89	-0.22	—	28.3	27.0	40.6	34.6	62.2
4318.65	Ca I	1.89	-0.21	—	38.7	40.2	39.1	47.9	50.4
4425.44	Ca I	1.88	-0.36	14.2	26.6	32.9	35.7	26.9	28.5
4454.78	Ca I	1.90	0.26	50.4	51.6	23.2	60.7	42.5	70.0
4455.89	Ca I	1.90	-0.53	17.1	30.3	—	—	15.4	27.3
5261.71	Ca I	2.52	-0.58	2.7	—	—	9.1	8.5	—
5265.56	Ca I	2.52	-0.11	7.5	21.1	—	17.1	17.8	17.5
5512.98	Ca I	2.93	-0.45	2.4	3.4	—	1.8	—	—
5581.97	Ca I	2.52	-0.56	2.0	9.0	—	5.4	10.8	16.1
5588.76	Ca I	2.53	0.36	—	40.2	—	32.5	31.8	50.7
5590.12	Ca I	2.52	-0.57	3.8	7.9	—	7.5	2.3	16.5
5594.47	Ca I	2.52	0.10	15.0	23.5	—	1.1	29.4	54.5

NOTE—(This table is available in machine-readable form.)

Table 3. Stellar Parameters of the Program Stars.

ID	Lick/APF (corrected & adopted)				Lick/APF (spectroscopic)				Photometry		Gaia DR2
	T_{eff}	$\log g$	[Fe/H]	ξ	T_{eff}	$\log g$	[Fe/H]	ξ	T_{eff} (V-J)	T_{eff} (V-K)	$\log g$
	(K)	(cgs)		(kms^{-1})	(K)	(cgs)		(kms^{-1})	(K)	(K)	(cgs)
J0326+0202	5080	2.03	-3.11	2.01	4900	1.59	-3.26	1.92	5083	5187	2.06
J1108+2530	5003	2.05	-2.72	1.08	4815	1.52	-2.89	1.09	5136	5141	2.15
J1256+3440	5215	1.74	-2.76	2.37	5050	1.36	-2.89	2.30	5074	5142	1.87
J1413+1727	4914	1.25	-3.00	1.92	4716	0.72	-3.20	2.02	4709	4704	1.23
J1630+0953	4783	1.02	-2.94	2.14	4570	0.40	-3.04	2.28	4693	4723	1.30
J2216+0246	4945	1.53	-2.52	1.68	4750	1.05	-2.67	1.67	4899	4936	1.87

Table 4. LTE Abundances of Individual Elements for the Program Stars

	J0326+0202				J1108+2530				J1256+3440			
	$\log \epsilon(X)$	[X/Fe]	σ	N	$\log \epsilon(X)$	[X/Fe]	σ	N	$\log \epsilon(X)$	[X/Fe]	σ	N
C(CH)	5.56	0.24	0.04	2	5.99	0.28	0.05	2	6.04	0.37	0.05	2
(CH) _{corr}	...	0.02	0.04	0.24
(CH) _{natal}	...	0.26	0.32	0.61
N(CN)
Na I	3.43	0.30	0.18	3	3.54	0.02	0.03	2	3.64	0.19	0.14	2
Mg I	5.11	0.62	0.16	5	5.26	0.38	0.16	6	5.09	0.28	0.12	4
Ca I	3.52	0.29	0.14	18	3.81	0.19	0.13	20	3.77	0.19	0.11	11
Sc II	0.26	0.22	0.13	6	0.36	-0.07	0.11	13	0.34	-0.05	0.18	9
Ti I	2.24	0.40	0.09	15	2.32	0.09	0.12	19	2.51	0.32	0.19	13
Ti II	2.06	0.22	0.11	28	2.06	-0.17	0.17	33	2.25	0.06	0.15	27
V I	0.71	-0.11	0.12	1	0.67	-0.54	0.11	1	1.01	-0.16	0.10	1
Cr I	2.51	-0.02	0.08	7	2.49	-0.43	0.16	12	2.63	-0.25	0.16	7
Mn I	2.07	-0.25	0.12	2	2.23	-0.48	0.11	3	2.32	-0.35	0.12	1
Fe I	4.39	0.00	0.16	118	4.78	-0.00	0.12	131	4.74	0.00	0.16	123
Fe II	4.38	-0.01	0.18	13	4.77	-0.01	0.12	20	4.74	0.00	0.15	14
Co I	2.41	0.53	0.12	2	2.14	-0.13	0.15	3	2.38	0.15	0.10	1
Ni I	3.38	0.27	0.18	7	3.46	-0.04	0.17	12	3.70	0.24	0.19	6
Zn I	1.77	0.32	0.13	1	1.75	-0.09	0.17	2	2.12	0.32	0.11	1
Sr II	-0.65	-0.41	0.11	1	-0.06	-0.21	0.19	1	-0.46	-0.57	0.11	1
Y II	-1.00	-0.10	0.08	1	-1.14	-0.63	0.11	3	-1.05	-0.50	0.12	1
Zr II	-0.36	0.17	0.15	1	-0.78	-0.64	0.14	4
Ba II	-1.48	-0.55	0.18	2	-0.76	-0.22	0.13	2	-1.25	-0.67	0.19	3
La II	-1.13	0.01	0.22	2	-1.01	0.65	0.20	2
Ce II	-1.88	-0.35	0.13	1	-2.10	-0.10	0.20	1	-1.57	-0.39	0.22	2
Nd II	-1.47	0.22	0.15	1	-1.13	0.21	0.15	2
Sm II	-1.25	0.50	0.19	3	-1.79	0.01	0.14	1
Eu II	< -2.60	-0.01	0.13	1	-2.35	-0.15	0.11	1	< -2.10	0.14	0.14	1

Table 4. Continued.

	J1413+1727				J1630+0953				J2216+0246			
	$\log \epsilon(X)$	$[X/Fe]$	σ	N	$\log \epsilon(X)$	$[X/Fe]$	σ	N	$\log \epsilon(X)$	$[X/Fe]$	σ	N
C(CH)	5.14	-0.29	0.07	2	6.13	0.64	0.05	2	6.19	0.28	0.09	2
(CH) <i>corr</i>	...	0.65	0.62	0.42
(CH) <i>natal</i>	...	0.36	1.26	0.70
N(CN)	5.77	0.88	0.17	1
Na I	3.58	0.34	0.13	3	3.50	0.20	0.11	2	3.76	0.04	0.15	3
Mg I	4.96	0.36	0.16	2	5.22	0.56	0.12	5	5.50	0.42	0.12	6
Ca I	3.69	0.35	0.18	11	3.61	0.21	0.19	18	4.08	0.26	0.12	17
Sc II	0.30	0.15	0.17	7	0.20	-0.01	0.13	10	0.59	-0.05	0.18	9
Ti I	2.27	0.32	0.11	9	2.22	0.21	0.17	14	2.66	0.23	0.12	14
Ti II	2.25	0.30	0.12	14	2.23	0.22	0.13	28	2.34	-0.09	0.13	32
V I	0.88	-0.05	0.16	1	1.10	0.11	0.15	1	0.89	-0.53	0.15	1
Cr I	2.76	0.12	0.11	6	2.67	-0.01	0.16	8	3.01	-0.11	0.17	7
Mn I	2.33	-0.10	0.10	1	2.23	-0.26	0.16	1	2.47	-0.44	0.13	2
Fe I	4.50	0.00	0.19	119	4.56	-0.00	0.15	127	4.97	-0.01	0.15	139
Fe II	4.50	0.00	0.17	11	4.56	-0.00	0.17	12	4.98	-0.01	0.19	14
Co I	2.22	0.23	0.11	2	2.61	0.56	0.12	1	2.42	-0.05	0.19	2
Ni I	3.20	-0.02	0.17	7	3.34	0.06	0.18	9	3.63	-0.07	0.17	10
Zn I	1.88	0.32	0.13	1	2.04	0.42	0.13	1	2.25	0.21	0.19	1
Sr II	-0.06	-0.07	0.20	1	-0.73	-0.66	0.12	1	-0.29	-0.64	0.17	1
Y II	-1.50	-0.38	0.19	1	-1.25	-0.52	0.14	1	-0.44	-0.13	0.13	2
Zr II	-0.32	0.04	0.16	1	-0.26	-0.32	0.16	1
Ba II	-1.09	-0.27	0.19	3	-0.95	-0.19	0.19	3	-0.43	-0.09	0.22	3
La II	-1.99	-0.15	0.14	1	-1.04	0.39	0.16	2
Ce II	-1.62	0.13	0.20	3	-1.40	-0.04	0.19	1	-0.97	-0.03	0.20	1
Nd II	-1.41	0.50	0.19	9	-1.45	0.07	0.28	2	-1.58	-0.48	0.17	4
Sm II	-2.00	0.37	0.26	2	-1.81	0.17	0.15	1
Eu II	< -2.35	0.13	0.16	1	< -2.35	0.07	0.15	1	< -2.00	0.00	0.19	1

NOTE—N refers to the number of lines adopted for determination of the elemental abundances.

Table 5. Estimated Abundance Uncertainties in the Element Abundance Ratios [X/Fe] for J1630+0953. The Other Sample Stars Yield Quite Similar Results.

Element	Ion	Random error	ΔT_{eff} +100 K	$\Delta \log g$ +0.3 dex	Δv_{micr} +0.3 km s ⁻¹	Root Mean Square
C	CH	0.05	0.19	0.11	0.00	0.23
N	NH	0.17	0.22	0.11	0.00	0.30
Na	1	0.11	0.09	-0.01	-0.02	0.14
Mg	1	0.12	0.09	-0.06	0.06	0.17
Ca	1	0.19	0.08	-0.01	-0.03	0.21
Sc	2	0.13	0.07	0.11	-0.02	0.19
Ti	1	0.17	0.10	-0.01	-0.01	0.19
Ti	2	0.13	0.04	0.08	-0.12	0.19
V	2	0.15	0.05	0.10	0.00	0.19
Cr	1	0.16	0.12	-0.01	-0.03	0.20
Mn	1	0.15	0.12	0.00	-0.01	0.19
Fe	1	0.17	0.12	-0.02	-0.08	0.18
Fe	2	0.12	0.02	0.11	-0.01	0.16
Co	1	0.12	0.12	0.00	-0.03	0.17
Ni	1	0.18	0.15	-0.03	-0.01	0.20

NOTE—Random errors represent the standard error of the mean and the last column represent the root mean squares of these errors.

Table 6. Parallaxes, Proper Motions and Distances

Star	<i>Gaia</i> DR2 source ID	ϖ error (mas)	pmra error (mas yr ⁻¹)	pmdec error (mas yr ⁻¹)	Distance d1 d2 (kpc)
J0326+0202	3268028903151246720	0.5421 0.0392	22.759 0.074	-14.128 0.062	1.727 1.617 1.853
J1108+2530	3995801795674031616	0.4887 0.0423	0.553 0.089	-38.926 0.062	1.893 1.753 2.057
J1256+3440	1515900293283319168	0.1945 0.0469	4.068 0.058	-13.785 0.048	3.601 3.134 4.194
J1413+1727	1233499867083517952	0.1525 0.0488	-6.039 0.089	-10.405 0.095	4.240 3.590 5.100
J1630+0953	4458577516730343424	0.1170 0.0261	-8.735 0.033	-8.939 0.023	6.183 5.354 7.267
J2216+0246	2682719929806900096	0.2893 0.0530	8.700 0.090	-11.429 0.100	2.899 2.521 3.391

NOTE—The d1 and d2 columns indicate the 16th percentile and 84th percentile confidence intervals.

Table 7. Positions and Galactic Space-velocity Components.

Star	X	Y	Z	U	V	W	V_R	V_ϕ	V_\perp
	(kpc)			(km s ⁻¹)			(km s ⁻¹)		
J0326+0202	9.47 ^{+0.08} _{-0.08}	0.03 ^{+0.00} _{-0.00}	-1.15 ^{+0.08} _{-0.07}	-115.54 ^{+2.84} _{-2.79}	-201.44 ^{+13.81} _{-13.13}	-22.65 ^{+3.24} _{-3.39}	-115.55 ^{+2.84} _{-2.79}	201.44 ^{+13.13} _{-13.81}	117.74 ^{+4.31} _{-4.39}
J1108+2530	8.83 ^{+0.05} _{-0.05}	0.38 ^{+0.03} _{-0.03}	1.77 ^{+0.13} _{-0.13}	183.79 ^{+9.97} _{-10.14}	-287.20 ^{+24.04} _{-23.70}	-120.18 ^{+1.86} _{-1.89}	183.57 ^{+9.94} _{-10.10}	287.33 ^{+23.72} _{-24.05}	219.41 ^{+10.11} _{-10.27}
J1256+3440	8.40 ^{+0.03} _{-0.03}	-0.43 ^{+0.06} _{-0.06}	3.59 ^{+0.46} _{-0.47}	182.38 ^{+23.98} _{-24.38}	-110.44 ^{+20.46} _{-19.99}	317.44 ^{+3.91} _{-3.86}	182.48 ^{+24.02} _{-24.40}	110.27 ^{+19.95} _{-20.42}	366.15 ^{+24.34} _{-24.70}
J1413+1727	6.69 ^{+0.23} _{-0.23}	-0.27 ^{+0.04} _{-0.04}	3.99 ^{+0.60} _{-0.60}	92.72 ^{+7.03} _{-6.93}	-220.29 ^{+36.13} _{-35.81}	104.85 ^{+0.87} _{-0.90}	92.875 ^{+7.08} _{-6.98}	220.23 ^{+35.80} _{-36.11}	140.07 ^{+7.13} _{-7.04}
J1630+0953	3.67 ^{+0.60} _{-0.62}	-2.15 ^{+0.28} _{-0.29}	3.63 ^{+0.49} _{-0.47}	142.91 ^{+12.36} _{-11.93}	-311.69 ^{+44.89} _{-46.83}	131.88 ^{+12.42} _{-12.03}	145.78 ^{+13.76} _{-12.88}	310.35 ^{+46.32} _{-44.49}	196.58 ^{+18.54} _{-17.62}
J2216+0246	7.31 ^{+0.12} _{-0.12}	-1.96 ^{+0.26} _{-0.26}	-1.93 ^{+0.25} _{-0.25}	-37.84 ^{+2.70} _{-2.79}	-187.73 ^{+17.67} _{-17.68}	-72.86 ^{+18.67} _{-18.72}	-36.98 ^{+2.54} _{-2.60}	187.90 ^{+17.70} _{-17.70}	81.71 ^{+18.84} _{-18.90}

NOTE—The - and + indicate the 16th percentile and 84th percentiles

Table 8. Calculated Orbital Parameters, Energies and Angular Momenta.

Star	r_{apo}	r_{peri}	Z_{max}	e	E	L_Z
	(kpc)				$(10^3 \text{km}^2 \text{s}^{-2})$	(kpc km s^{-1})
J0326+0202	$10.88^{+0.18}_{-0.16}$	$0.42^{+0.30}_{-0.26}$	$1.35^{+0.05}_{-0.03}$	$0.93^{+0.05}_{-0.05}$	$-0.98^{+0.03}_{-0.03}$	$-214.66^{+29.32}_{-30.21}$
J1108+2530	$15.65^{+1.73}_{-1.31}$	$1.91^{+0.57}_{-0.60}$	$7.43^{+0.23}_{-0.26}$	$0.78^{+0.05}_{-0.03}$	$-0.60^{+0.09}_{-0.09}$	$-1061.80^{+21.31}_{-22.01}$
J1256+3440	$65.94^{+14.83}_{-9.67}$	$8.90^{+0.21}_{-0.19}$	$29.69^{+4.02}_{-2.62}$	$0.76^{+0.04}_{-0.03}$	$-0.52^{+0.08}_{-0.07}$	$2666.88^{+41.09}_{-40.83}$
J1413+1727	$8.03^{+0.10}_{-0.08}$	$2.88^{+0.74}_{-0.25}$	$7.90^{+0.12}_{-0.50}$	$0.47^{+0.03}_{-0.09}$	$-0.91^{+0.09}_{-0.08}$	$700.25^{+25.89}_{-25.67}$
J1630+0953	$7.11^{+2.54}_{-0.69}$	$4.16^{+0.82}_{-1.23}$	$7.11^{+2.50}_{-0.72}$	$0.30^{+0.11}_{-0.04}$	$-1.18^{+0.02}_{-0.02}$	$559.86^{+5.63}_{-5.21}$
J2216+0246	$8.07^{+0.11}_{-0.12}$	$0.47^{+0.60}_{-0.25}$	$3.57^{+2.46}_{-0.92}$	$0.89^{+0.06}_{-0.13}$	$-1.14^{+0.05}_{-0.04}$	$-551.44^{+138.48}_{-137.99}$

NOTE—The – and + indicate the 16th percentile and 84th percentiles

